Development of Fe-based Metallic Glass for Corrosion-Resistant Applications

Dissertation submitted to
Visvesvaraya National Institute of Technology, Nagpur
in partial fulfillment of the requirements for the award of
the degree

Master of Technology
in
Process Metallurgy

by

Ritik Khushal Nakhate
(MT23PME002)

under the guidance of

Dr. Anil Kumar **Dr. Amrut Vijay Agasti**

Department of Metallurgical and Materials Engineering
Visvesvaraya National Institute of Technology
Nagpur 440 010 (India)

June 2025

Development of Fe-based Metallic Glass for Corrosion-Resistant Applications

Dissertation submitted to
Visvesvaraya National Institute of Technology, Nagpur
in partial fulfillment of the requirements for the award of
the degree

Master of Technology
in
Process Metallurgy

by
Ritik Khushal Nakhate
(MT23PME002)

under the guidance of

Dr. Anil Kumar **Dr. Amrut Vijay Agasti**

Department of Metallurgical and Materials Engineering
Visvesvaraya National Institute of Technology
Nagpur 440 010 (India)

June 2025

© Visvesvaraya National Institute of Technology (VNIT) 2025

Department of Metallurgical and Materials Engineering
Visvesvaraya National Institute of Technology, Nagpur

Declaration

I, Ritik Khushal Nakhate, hereby declare that this dissertation titled "Development of Fe-based Metallic Glass for Corrosion Resistant Applications" was carried out by me in the Department of Metallurgical and Materials Engineering of Visvesvaraya National Institute of Technology, Nagpur. The work is original and has not been submitted earlier whole or in part for the award of any degree/diploma at this or any other Institution / University.

RITIK KHUSHAL NAKHATE
Date:

Certificate

This certifies that the dissertation titled "Development of Fe-based Metallic Glass for Corrosion Resistant Applications" is submitted by **Ritik Khushal Nakhate** in partial fulfillment of the requirements for the award of the degree of **Master of Technology in Process Metallurgy**, VNIT Nagpur. The work is comprehensive, complete and fit for final evaluation.

Dr. Anil Kumar
Assistant Professor, MME, VNIT, Nagpur

Dr. Amrut V. Agasti
Assistant Professor, MME, VNIT, Nagpur

Dr. Dilip Ramkrishna Peshwe
Head, Department of Metallurgical and Materials Engineering
VNIT, Nagpur
Date:

NON-PLAGIARISM CERTIFICATE

Ritik K. Nakhate

ORIGINALITY REPORT

11%	7%	8%	2%
SIMILARITY INDEX	INTERNET SOURCES	PUBLICATIONS	STUDENT PAPERS

PRIMARY SOURCES

1	link.springer.com Internet Source	1%
2	www.mdpi.com Internet Source	1%
3	worldwidescience.org Internet Source	1%
4	Suryanarayana, . "Glass-Forming Ability of Alloys", Bulk Metallic Glasses, 2010. Publication	1%
5	Kasyap, Supriya. "Study of Structure, Thermodynamics and Phase Transformation in Zr-Based Amorphous Alloys", Maharaja Sayajirao University of Baroda (India), 2020 Publication	1%
6	Anil Kumar, Rahul Kumar, Pavan Bijalwan,	<1%

ACKNOWLEDGEMENT

It is with great respect and gratitude that I take this opportunity to acknowledge the individuals and institutions whose support, guidance, and encouragement have made the successful completion of this thesis possible.

First and foremost, I would like to express my deepest appreciation to my research supervisors, **Dr. Anil Kumar and Dr. Amrut V. Agusti**, for their constant support, expert guidance, and constructive feedback throughout every stage of this work. Their deep knowledge, critical insights, and encouragement have been invaluable in shaping the course of this research. I am truly grateful for the patience, motivation, and inspiration they have extended, even during the most challenging phases of this study.

I am equally thankful to the **faculty members of the Department of Metallurgical and Materials Engineering**, Visvesvaraya National Institute of Technology, Nagpur, for their academic mentorship and the valuable knowledge imparted to me over the years. Their dedication to teaching and research has had a profound influence on my academic growth and professional development.

I would like to extend special thanks to the **technical and laboratory staff** for their assistance in the experimental and analytical phases of my work. Their support in managing equipment, ensuring lab safety, and maintaining resources was crucial to the smooth execution of my research activities.

I am also grateful to **my fellow researchers, colleagues, and friends in the lab** for their camaraderie, insightful discussions, and collaboration. The shared experiences, whether academic or personal, have enriched my time during this research journey and contributed immensely to my learning.

My sincere thanks go to **the authors and scholars** whose research laid the foundation for my study. Their published work provided not only valuable information but also the inspiration to explore and contribute to the field of Fe-based metallic glasses and corrosion science.

On a more personal note, I would like to express my heartfelt gratitude to **my family**. Their unconditional love, patience, and moral support have been my anchor throughout this academic journey. To my parents, whose values and sacrifices laid the foundation of my education, and to my siblings and loved ones for their constant encouragement—I am forever indebted.

Last but not least, I am thankful to everyone who, directly or indirectly, contributed to the successful completion of this thesis. Your encouragement and belief in my work have been deeply motivating and have helped me reach this important milestone.

ABSTRACT

The present study focuses on the development and evaluation of corrosion-resistant Fe-based metallic glass coatings and ribbons incorporating low-chromium and economically viable alloying elements. Two alloy systems—$Fe_{73}Cr_2Si_{11}B_{11}C_3$ and $Fe_{80}Cr_{10}B_4C_2P_4$ (atomic percent) were selected owing to their high glass-forming ability, cost-effectiveness, and favourable mechanical and electrochemical characteristics. These powered alloys were deposited onto mild steel substrates using Atmospheric Plasma Spraying (APS) under varying thermal input conditions, corresponding to plasma power settings of 25 kW, 30 kW, and 35 kW, to systematically study the influence of process parameters on coating microstructure, phase evolution, and corrosion behaviour. Microstructural characterisation using scanning electron microscopy (SEM)revealed that coatings deposited at elevated plasma powers exhibited improved inter-splat bonding and reduced porosity due to enhanced particle melting and splat fusion. However, a concomitant increase in plasma power was also found to promote partial devitrification, leading to the emergence of crystalline α-Fe phases at the expense of the amorphous matrix.

Electrochemical performance was evaluated using potentiodynamic polarization and electrochemical impedance spectroscopy (EIS) in a 3.5 wt.% NaCl solution, simulating a marine chloride environment. Among the coatings tested, the sample deposited at 30 kW (Coating 2) demonstrated the most favourable corrosion resistance, marked by the lowest corrosion current density (9.7 $\mu A/cm^2$) and the most noble corrosion potential (−485 mV). To further understand the corrosion mechanisms, Raman spectroscopy was employed on corroded surfaces, revealing the formation of iron oxide species, notably γ-Fe_2O_3, which is associated with enhanced passivation. In contrast, coatings produced at 25 kW and 35 kW exhibited either excessive porosity or increased crystallinity, both of which compromised corrosion resistance. For comparison, a melt-spun ribbon of $Fe_{80}Cr_{10}B_4C_2P_4$ was also fabricated under controlled argon atmosphere using rapid solidification. The ribbon exhibited a fully amorphous structure and superior corrosion resistance, with a corrosion current density as low as 0.10 $\mu A/cm^2$, attributed to the absence of crystalline phases and uniform microstructure.

LIST OF FIGURES

Figure No.	Title	Page no.
1.1	Image comparing different metallic glasses (a) Metallic Glasses Ribbon and (b) Bulk Metallic Glasses [35].	3
2.1	Illustrative time–temperature–transformation (T–T–T) diagram for an example alloy system.	7
2.2	Schematic diagram of Gas Atomization process [49].	12
2.3	Schematic diagram of Water Atomization process [49].	13
2.4	Schematic diagram of Atmospheric Plasma Spraying process [12].	14
2.5	Schematic diagram of Melt spun process [50].	15
2.6	(a) A magnetic yoke fabricated using an $Fe_{73}Ga_4P_{11}C_5B_4Si_3$ bulk metallic glass plate for use in a prototype linear actuator. and (b) Shot Peening Balls.	17
2.7	(a) Potentiodynamic polarization curves in 3.5 wt% NaCl solution at room temperature for $Fe_{54}M_5Cr_{15}Mo_6Si_2B_4P_{10}C_4$ glassy alloy rods and 316L stainless steel; (b) Nyquist plots $Fe_{54}M_5Cr_{15}Mo_6Si_2B_4P_{10}C_4$ glassy alloy rods and 316L in 3.5 wt.% NaCl solution at room temperature [21].	18
3.1	Electrochemical Testing Equipment.	23
4.1	(a) SEM image displays Fe-based feedstock powder with a spherical shape, (b) XRD pattern shows a broad and hollow peak indicative of its amorphous nature.	27
4.2	SEM images displaying (a-d) top as-sprayed surfaces and (e-h) cross-sectional surfaces of the coatings.	28
4.3	XRD patterns of different coatings (a) and Ribbons (b) show differences in their crystallization.	29
4.4	Potentiodynamic polarization curves of coated samples.	30
4.5	Electrochemical impedance plots of coatings deposited at different plasma power and expose to 3.5% NaCl solution. (a) Nyquist plot, (b) Bode impedance plot, (c) Bode phase angle plot.	31-32

Figure No.	Title	Page no.
4.6	Raman spectra of coating displaying characteristic peaks of various oxides and hydroxides phases.	33
4.7	Potentiodynamic polarization curves of the Ribbon sample.	35
4.8	EIS Nyquist plot of Ribbon samples exposed to 3.5% NaCl solution.	35
4.9	EIS Bode impedance plot of Ribbon samples exposed to 3.5% NaCl solution.	36
4.10	EIS Bode phase angle plot of Ribbon samples exposed to 3.5% NaCl solution.	36
4.11	Raman spectra of the coating Ribbon sample displaying characteristic peaks of various oxides and hydroxide phases.	37
4.12	Potentiodynamic polarization curves of coated samples and the Ribbon sample.	38
4.13	EIS Nyquist plot of coatings and ribbon exposed to 3.5% NaCl solution.	39
414	EIS Bode impedance plot of coatings and ribbon exposed to 3.5% NaCl solution.	39
4.15	EIS Bode phase angle plot of coatings and ribbon exposed to 3.5% NaCl solution.	40
4.16	Raman spectra of coating 2, 4, and Ribbon sample displaying characteristic peaks of various oxides and hydroxide phases.	41
4.17	SEM micrographs of the surface of Fe-based (a-d) coatings and (e-g) ribbons.	42

List of Tables

Table No.	Title	Page No.
2.1	Representative Critical Cooling Rate (Rc) of Fe-based Metallic Glasses [5].	8
2.2	Electrochemical parameters derived from potentiodynamic polarization curves [21].	19
2.3	Effect of alloying elements on the Corrosion Resistance property [5].	19
3.1	Factors utilized for applying Fe-based nanocrystalline/ amorphous coatings through Atmospheric Plasma Spraying (APS).	22
3.2	Factors utilized for manufacturing Fe-based ribbon through melt spun.	22

LIST OF PUBLICATIONS

1. **Nakhate R. K.**, Rohilla G., Faridi M. A., Agasti A. V., Laha T., Kumar A., Evaluation of corrosion behavior of plasma sprayed low Cr containing Fe-based ($Fe_{73}Cr_2Si_{11}B_{11}C_3$) amorphous/ crystalline coating., Structural Integrity Procedia (accepted).

INDEX

Chapter	Title	Page number
1	**Introduction**	**1**
1.1	Motivation and challenges for synthesising Metallic Glass	2
1.2	Importance of Fe-Based Metallic Glass	3
1.3	Objective	4
2	**Literature Survey**	**5**
2.1	History of Metallic glasses	6
2.2	Fundamentals of Metallic Glasses	7
2.3	Fe-Based Metallic Glasses	8
2.4	Glass-Forming Ability and Its Importance	8
2.5	Synthesis of Metallic glasses	11
2.6	Applications of Fe-based Metallic glass	16
2.7	Corrosion Behaviour of Fe-based MG	17
2.8	Material selection	19
3	**Experimental Procedure**	**21**
3.1	Synthesis of Metallic Glasses Coatings and Ribbons	22
3.2	Characterization and Testing Methods	22
3.3	Electrochemical Testing	23
4	**Results and Discussion**	**26**
4.1	Phase Analysis and Microstructural Characterization	27
4.2	Electrochemical Behaviour	30
4.3	Raman Analysis	33

Chapter	Title	Page number
4.4	Ribbon Corrosion Study	34
4.5	Comparative Analysis	37
5	**Conclusion**	**44**
5.1	Summary of Key Finding	45
5.2	Future Work	46
6	**References**	**47**

CHAPTER 1

1.Introduction

1.1.Motivation and challenges for synthesising Metallic Glass

Metallic glasses, referred to as amorphous metals, represent a class of alloys that are devoid of the crystalline architecture characteristic of the majority of metallic substances. Instead of possessing a systematic, periodic atomic arrangement, the constituents of metallic glasses are distributed in a stochastic manner, analogous to the atomic configuration observed in traditional glasses (such as those used in windows). Contrasting with crystalline metals, which are defined by a regular and repetitive atomic configuration, metallic glasses showcase a disordered atomic layout wherein atoms are arranged in a random, non-repetitive manner, echoing the structural properties associated with silica (SiO_2) glasses [5-8]. The absence of a crystalline framework in metallic glasses engenders a suite of unique properties. These materials display an extraordinary amalgamation of strength, hardness, and ductility, concurrently demonstrating superior resistance to wear and corrosion. Such attributes render them particularly advantageous for various high-tech applications [5]. The amorphous characteristic of these glasses eliminates grain boundaries, which frequently act as failure points in crystalline materials, thereby enhancing mechanical properties that include remarkable tensile strength, elevated elastic limits, and superior fatigue resistance.

The creation of metallic glasses usually takes place through the rapid cooling (quenching) of molten metal mixtures at rates surpassing the time needed for crystallization (often greater than 10^6 K/s). This swift cooling process hinders the development of crystalline structures and enables the atoms to solidify in a disordered arrangement. The potential to create metallic glasses hinges on various elements, including the composition of the alloy and the rate at which it cools [5-7]. Commonly used metallic glass-forming alloys are typically blends of metals like iron, nickel, titanium, and zirconium. Brittleness and the inability to freely deform into complex shapes are some of the challenges faced by metallic glasses, despite possessing remarkable mechanical properties. This is a result of the inability to undergo plastic deformation, which is characteristic of crystalline metals. Regardless, the distinctive traits of metallic glasses have sparked interest in their application for high-performance protective coatings. Work being done towards new alloy compositions is coupled with developing innovative methods of manufacturing, of metallic glass [25-28].

Bulk Metallic Glasses (BMGs) are a unique class of metallic materials characterized by their non-crystalline atomic structure, formed through rapid cooling from the liquid state. In contrast to earlier metallic glasses, which could only be produced in very thin forms due to their high cooling rate requirements, BMGs are noted for their comparatively larger section thickness. Typically, a metallic glass is classified as "bulk" if its thickness is at least 1 mm, though some researchers advocate for a minimum of 10 mm as a more accurate definition [5]. The pursuit of metallic glasses with larger dimensions for broader industrial use led to the development of BMGs, which can be fabricated at slower cooling rates on the order of 10^3 K/s or lower. This contrasts with the significantly faster cooling needed to produce thin ribbons. Interest in this material class grew rapidly after the successful creation of bulk forms in the late 1980s, marking a major milestone in the advancement of amorphous metal technologies [5]. On the other hand, the only practical form in which amorphous metallic alloys could be consistently produced from the liquid state using the

available rapid solidification techniques is Metallic Glasses Ribbon. The rapid solidification is only possible when the material is thin or one of the dimensions is thin (between 20-50 μm). One of such products is Metallic Glass Ribbon. A product can be called as a metallic glass ribbon when it is a thin, continuous strip, typically with a thickness in the range of 20-50 μm (or 15-50 μm) and width of 2-5 mm (or 0.05-0.5 mm), produced by rapid solidification processing methods like melt spinning, resulting in a glassy, nanocrystalline structure [5].

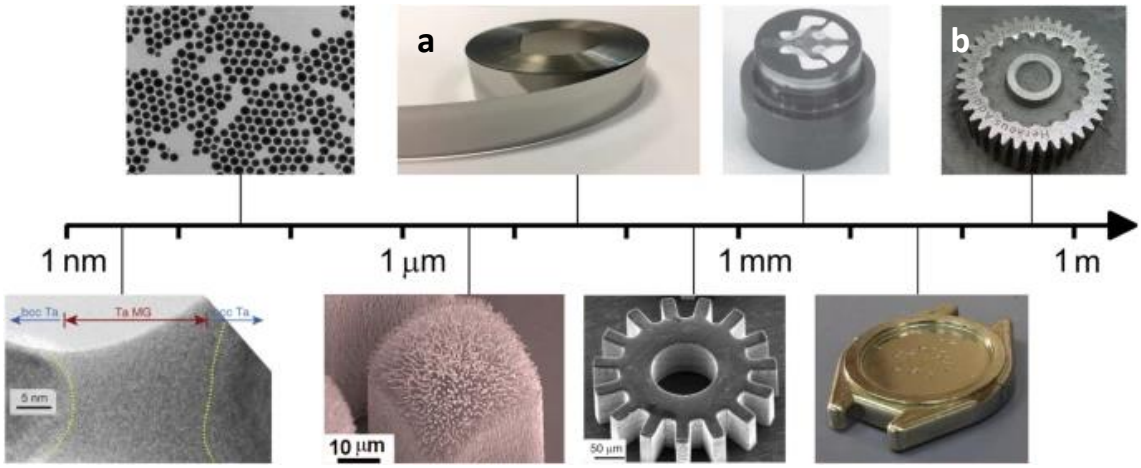

Figure 1.1: Image comparing different metallic glasses (a) Metallic Glasses Ribbon and (b) Bulk Metallic Glasses [35].

1.1. Importance of Fe-Based MG

Fe-based metallic glasses contribute meaningfully to environmental sustainability through their inherent material properties and long-term performance advantages. One of their most notable environmental benefits stems from their high corrosion resistance, which enables components coated with or made from these materials to withstand harsh environmental conditions without rapid degradation [25]. This resistance reduces the frequency of part replacements, thereby lowering the overall consumption of raw materials and minimizing industrial waste. In addition, the decreased servicing needed for these components boosts their longevity, which in turn lessens the environmental impact related to manufacturing, transporting, or disposing of damaged components. Fe-based metallic glasses, for example, are them in marine engineering, as well as infrastructure and energy, where exposure to the environment is critical [19]. This, in turn, leads to fewer maintenance works and lower material turnover. Consequently, the energy and emissions involved in frequent repairs and replacements are tremendously reduced.

Cost-effective Fe-based metallic glasses are one of the reasons why they are gaining interest in industrial applications. Heavily based on iron as a compound, it also becomes economically advantageous due to the ease and low cost of acquiring iron resources as opposed to other auxiliary metals that are rare or precious [12]. Therefore, this encourages easy manufacturing alongside practical incorporation within a wide range of sectors without imposing excessive financial burdens. The substantial performance-to-cost ratio of Fe-based metallic glasses allows industries to harness benefits from the advanced material properties of high strength, exceptional wear and corrosion resistance, without

incurring the high costs of materials and processing that are frequently associated with other advanced alloys. This economic advantage enhances their suitability for cost-sensitive applications in developing regions where affordability and longevity are critical [19]. Moreover, the reduced maintenance and replacement expenditures incur additional economic benefits. Since components made from or coated with Fe-based metallic glasses require less frequent repairs due to better longevity and resistance to degradation, operational costs decrease. This has a greater impact in transportation, construction, and power generation industries [16].

1.3. Objective

1. To develop Fe-based metallic glass compositions with improved corrosion resistance suitable for saline environments.
2. To investigate the effect of microstructural features contributing to corrosion resistance
3. To evaluate the effects of key processing factors like Plasma Power on the structural and corrosion properties of the metallic glasses.

CHAPTER 2

2. Literature Survey

2.1. History of Metallic glasses

The intriguing history of metallic glasses, or amorphous metals, stretches over sixty years and encompasses significant discoveries, technological progress, and enhanced insights into materials science. Their story began in the 1950s. In 1960, a team made the first metallic glass. They quickly cooled gold and silicon, stopping crystal formation. This discovery was doubted at first. People thought metals had to be crystalline [5]. Interest grew in the 1970s. New iron-based alloys showed better strength. Yet, making large amounts was still hard. By the 1980s, methods like melt-spinning made thin ribbons possible. The real change came in the early 1990s. Researchers created bulk metallic glasses (BMGs). They used alloys of zirconium, titanium, copper, nickel, and beryllium. These BMGs were very strong and elastic. They also came in larger sizes. By the late 1990s, BMGs were sold commercially. They appeared in sports gear, medical tools, and electronics. Modern metallic glasses resist corrosion and wear. Their high strength suits them for gears and aerospace parts. Companies sell BMG products, like phone cases and golf clubs.

The corrosion behavior of metallic glasses has been a topic of scientific interest since the 1970s. Initial research focused on rapidly solidified alloy ribbons, particularly Fe-based systems produced via melt spinning. One of the earliest studies, conducted in 1974, highlighted that amorphous Fe-Cr-P-C alloys exhibited significantly superior corrosion resistance compared to their crystalline counterparts. For instance, in a 1 N NaCl solution at 30°C, these amorphous alloys showed negligible corrosion, whereas similar crystalline alloys corroded at rates between 0.5 to 1 mm/year. Interestingly, the chromium content needed to impart corrosion resistance was found to be lower (about 8 at.%) in the amorphous Fe-based alloys state than in the crystalline form (which required over 12 at.%). This early discovery was pivotal in establishing metallic glasses as promising materials for corrosive environments. Three primary factors were recognized as contributors to their high corrosion resistance:

1. **Chemical Homogeneity**: Due to the rapid cooling in melt-spinning, there was insufficient time for elemental segregation.
2. **Absence of Crystal Defects**: The lack of grain boundaries and second-phase particles eliminated potential initiation sites for localized corrosion.
3. **Uniform Passive Film Formation**: Glassy surfaces allowed for even distribution of passive films, reducing the need for high concentrations of corrosion-resistant elements

Later work showed that corrosion resistance in metallic glasses is significantly influenced by their microstructure. A fully amorphous structure generally offered better corrosion protection than either nanocrystalline composites or fully crystallized forms. Studies indicated that the presence of nanocrystals greater than about 20 nm could degrade corrosion performance due to incomplete passivation. However, very fine inclusions (around 2–3 nm) were less detrimental.

2.2. Fundamentals of Metallic Glasses

The transformation into a metallic glass occurs through continuous cooling from the liquid phase. During this process, the material bypasses crystallization due to kinetic constraints, resulting in an undercooled liquid that eventually transitions into a rigid glassy state. This transition happens at the glass transition temperature (Tg), which is not always easy to detect, especially under slow heating rates [5]. However, the absence of a Tg does not disqualify a material from being a glass if its structure is proven to be noncrystalline. Unlike crystals, metallic glasses do not have a unique, fixed structure. The atomic configuration in a metallic glass is determined by the cooling rate and changes over time due to structural relaxation. A key feature is the existence of a supercooled liquid region (SLR), defined by the temperature range between Tg and the crystallization temperature (Tx)[5]. Within this range, the material can exhibit reversible transitions between the glassy and supercooled liquid states. The critical cooling rate (Rc) refers to the minimum cooling rate needed to suppress crystallization and allow the formation of an amorphous solid. If the cooling rate is slower than the Rc, crystallization occurs, and a crystalline structure is formed. If the cooling rate is slower than the Rc, crystallization occurs, and a crystalline structure is formed as shown in Figure 1.2. In Fe-based metallic glasses, the Rc can vary depending on the specific alloy composition (Table 2.1), but it generally needs to be relatively high (i.e., rapid cooling) to achieve the desired amorphous state [29]. For example, alloys with higher concentrations of elements like boron and silicon often have lower critical cooling rates, meaning they can form glass more easily.

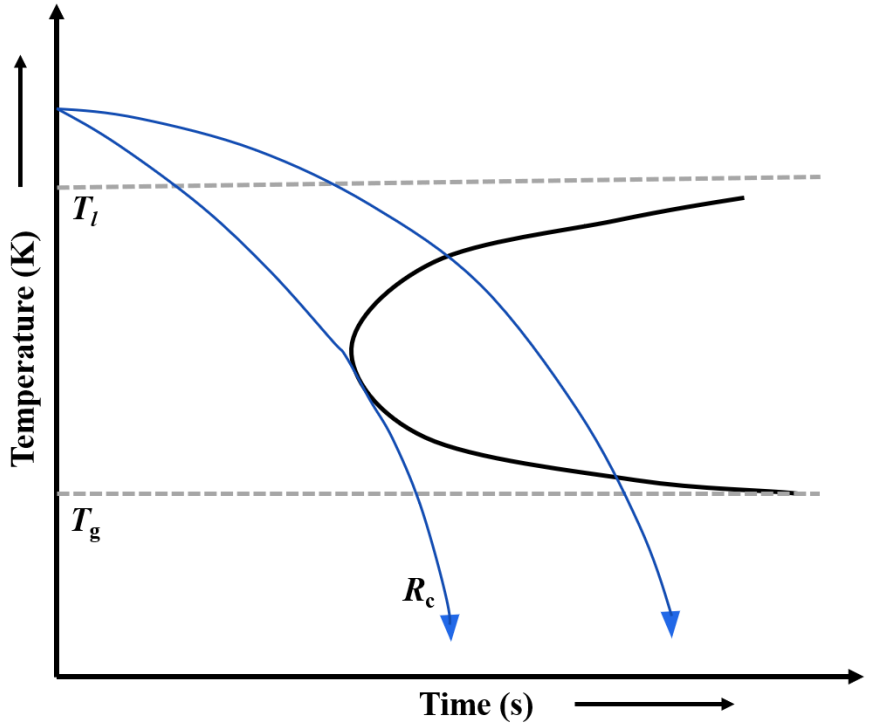

Figure 2.1: Illustrative time–temperature–transformation (T–T–T) diagram for an example alloy system.

Table 2.1: Representative Critical Cooling Rate (Rc) of Fe-based Metallic Glasses [5]

Alloy Composition	Rc (K s^{-1})
$Fe_{43}Cr_{16}Mo_{16}C_{10}B_5P_{10}$	100
$Fe_{40}Ni_{40}P_{14}B_6$	4.4×10^7

2.3. Fe-Based Metallic Glasses

Iron-based metallic glasses are an amorphous metal being, as the name indicates, a metallic glass material, part of the category of amorphous metals, produced from iron and different metals and metalloids (metals that are metal-like), to display a combination of properties and application capabilities; a departure from the crystalline atomic structure that usually defines metals and metallic alloys, as this material is produced by cooling the liquid metal so rapidly that the atoms will not be able to form an ordered, crystalline structure, as in most metals and alloys; in association with their disordered, amorphous structure, this group of materials represent a class of amorphous metal which are ideal for providing thermal insulation in power transformers for reducing heat dissipation, increasing heat flow, act as a thermal barrier, and acting as a thermal insulator [8]. Fe-based metallic glass is a unique material because of its amorphous atomic structure with remarkable properties including excellent tensile strength and hardness, and promising fordurable and wear-resistant applications [10]. The absence of grain boundaries makes them superior in tensile strength and resistance to plastic deformation, however can incur being brittle, losing ductility compared to crystalline metals. Furthermore, their remarkable hardness contributes to outstanding wear and abrasion resistance, valuable in high-stress applications like gears, cutting tools, and protective coatings [7].

Fe-based metallic glasses exhibit notable thermal stability, characterized by a glass transition temperature (Tg) between 300°C and 500°C and a crystallization temperature (Tx) ranging from 500°C to 700°C [34,36,38,46], which varies with the specific alloy, while they feature low thermal expansion and moderate electrical resistivity; their corrosion resistance surpasses that of crystalline iron but falls short compared to zirconium-based alloys, and although they present advantages like high strength, magnetic performance, and wear resistance, their brittleness poses challenges for traditional machining and limits their utility in harsh environments [5-10]. However, their thermal stability is still limited by the range between Tg and Tx, and any heating beyond this range risks crystallization.

Fe-based metallic glasses are notable for their magnetic characteristics, particularly some variants that display soft magnetic behaviour with low coercivity and high magnetic permeability, making them highly suitable for use in electrical and magnetic devices like transformers, inductors, and magnetic sensors, where efficient energy transfer and minimal losses are essential; additionally, their low hysteresis losses facilitate energy-efficient performance in magnetic cores as they do not hold significant magnetic energy once the external magnetic field is removed.

2.4. Glass-Forming Ability and Its Importance

Glass-forming ability (GFA) refers to a material's capacity to solidify into an amorphous structure, particularly through rapid cooling from its liquid state. It is crucial in the manufacturing of bulk metallic glasses (MGs), influencing their processing and suitability for various applications. This is especially true for specific alloys, such as Fe-based metallic glasses (Fe-MGs), whose unique properties significantly impact their GFA [15]. The glass-forming ability (GFA) of metallic alloys is fundamentally important because it determines whether an alloy can form a glassy, amorphous structure instead of crystallizing upon cooling. Alloys with high GFA can solidify into metallic glass at relatively lower cooling rates, which enables the fabrication of bulk metallic glasses (BMGs) with significant cross-sectional dimensions often in the millimeter to centimeter range rather than being restricted to thin ribbons or films [5]. This is essential for practical applications, as it allows components to be manufactured in structural forms. High GFA also reflects greater thermal stability, evidenced by a wider supercooled liquid region, which is crucial for processing, shaping, and preventing premature crystallization during thermal exposure. Furthermore, enhanced GFA is associated with more homogenous amorphous structures, which contribute to superior mechanical properties such as high strength, elasticity, and corrosion resistance. These properties are critical for advanced applications in aerospace, electronics, and biomedical devices. Thus, optimizing and understanding GFA is not only key to the synthesis of metallic glasses but also to harnessing their full technological potential [5].

2.4.1. Factors Influencing Glass-Forming Ability (GFA)

- **Composition of the Alloy:**
  - The chemical composition is one of the primary factors influencing the glass-forming ability. The combination of base metals (like iron) and alloying elements such as boron, carbon, silicon, and phosphorus plays a significant role in determining whether the material can form an amorphous structure.
  - Alloying elements: Elements such as boron, phosphorus, and silicon are commonly added to metallic glasses because they help increase the glass-forming ability. For instance, boron is particularly known for enhancing the GFA by lowering the nucleation rate during cooling, thereby reducing the likelihood of crystalline phases forming [5,29].
  - Wide composition range: For alloys like Fe-based MGs, a composition with a wide liquidus phase region (a wide range of temperatures where the material is in a liquid state) allows for easier cooling into an amorphous state.
- **Cooling Rate:**
  - The cooling rate is perhaps the most important factor influencing GFA. Rapid cooling is necessary to prevent crystallization and maintain the amorphous structure. For metallic glasses to form, the cooling rate needs to be fast enough to quench the molten metal before it has time to crystallizecrystalli [28].

- The required cooling rate for Fe-based MGs is typically on the order of 10^3 to 10^6 K/s, which is much faster than that required for crystalline materials [5]. If cooling is too slow, the atoms in the material will organize into a crystal lattice, making the structure crystalline instead of amorphous.

❖ **Critical Cooling Rate (Rc):**

One of the foundational metrics of GFA is the critical cooling rate, the minimum rate at which a molten alloy must be cooled to avoid crystallization. Glass formation is only possible when crystallization is suppressed such that the volume fraction of crystalline material remains extremely low (typically around 10^{-6}). Factors influencing Rc include:

- Viscosity of the undercooled liquid
- Entropy of fusion
- Liquidus temperature

Higher viscosity and lower liquidus temperatures reduce the required Rc, improving GFA [5-9].

2.4.2. Thermodynamic Considerations in GFA

Gibbs Free Energy

- In metallic glasses, the Gibbs free energy difference between the crystalline and amorphous phases is a key factor that affects GFA. The amorphous phase is generally less thermodynamically stable than the crystalline phase.
- The difference in free energy between the amorphous and crystalline phases influences the nucleation rate of crystals during cooling. A higher GFA corresponds to a larger difference in free energy, which means that the material can maintain its amorphous state more easily without transitioning to a crystalline structure.

2.4.3. Structural Factors in GFA

❖ **Atomic Size Distribution:**

- The atomic size distribution of the constituent elements in an alloy plays a significant role in its GFA. If the atomic size mismatch between the different elements is too large, the atoms will not be able to arrange themselves in a disordered fashion efficiently, hindering glass formation.
- A high degree of atomic size mismatch between the primary metal (e.g., Fe) and the alloying elements (e.g., boron or carbon) can promote glass formation because it increases the viscosity of the liquid and reduces the tendency for crystallization. This is why Fe-based MGs often have elements like boron that cause a high atomic size mismatch, leading to better glass-forming ability [20-22].

❖ **Bonding and Local Ordering:**

- The type of atomic bonding in a material influences its GFA. For metallic glasses, the metallic bonding between atoms must be strong enough to form

a stable disordered network but not so strong that it promotes crystallization.

- Elements like boron and phosphorus introduce network-forming bonds, which help stabilize the amorphous structure by preventing the atoms from arranging into a crystalline lattice. These elements reduce the short-range order in the liquid state, making it easier for the liquid to be rapidly cooled into a glass.

2.4.4. Improve GFA by Alloying Addition

- The GFA of Fe-based metallic glasses can be improved by adding specific alloying elements that promote the formation of an amorphous phase. Boron, for instance, lowers the nucleation rate of crystals, making it easier to obtain an amorphous structure [29].
- Phosphorus and silicon also enhance GFA by improving the stability of the amorphous phase. These elements are particularly effective in Fe-based alloys, as they reduce the tendency of the material to crystallize during cooling.

2.4.5. Glass-Forming Ability in Fe-Based Metallic Glasses

In Fe-based metallic glasses, the presence of boron and carbon significantly enhances glass-forming ability by decreasing crystallization and increasing viscosity during cooling, which aids in achieving better GFA; especially when compositions include both boron and silicon, these elements effectively stabilize the amorphous structure, although the high critical cooling rate required for Fe-based MGs compared to other metallic glasses presents challenges for producing larger bulk samples, necessitating rapid cooling; the unique combination of iron, boron, carbon, and occasionally silicon in these alloys endows them with desirable properties like elevated strength, wear resistance, and soft magnetic characteristics, making them well-suited for applications across electronics, automotive, and aerospace sectors [26].

2.4.5.1. Influence of alloying elements on GFA of Fe-based metallic glasses

In terms of composition, metallic glasses are generally classified into two categories: metal-metalloid and metal-metal alloys. In metal-metalloid metallic glasses, the metallic alloying elements typically constitute approximately 80 at.%, while the metalloid content is maintained around 20 at.% [5]. The alloying elements in this category may consist of either a single element or a combination of multiple elements [24]. In contrast, metal-metal metallic glasses do not have strict compositional constraints. The glass-forming ability (GFA) is significantly influenced by chemical interactions and atomic size disparities among the constituent elements. The impact of specific alloying elements on the GFA of Fe-based alloy systems is discussed below.

2.5. Synthesis of MG

2.5.1. Powder Making

2.5.1.1 Gas Atomization

Gas atomization is a widely employed technique for producing fine metallic glass powders, leveraging high-pressure gas to rapidly cool molten metal and preserve its amorphous structure. In this process, the molten metal, typically in the form of a carefully selected alloy, is first heated to its melting point in a furnace or induction system. The molten metal is then directed through a nozzle, where it is atomized by a stream of high-pressure inert gas, such as argon or nitrogen as shown in Fig. This high-pressure gas breaks the molten metal into small droplets, which rapidly cool and solidify into fine powder particles as they are carried by the gas flow. The cooling rate achieved in gas atomization is extremely fast—on the order of 10^6 to 10^7 K/s—which is essential for maintaining the amorphous (glass-like) nature of the metal, especially for alloys with high glass-forming ability [5]. Key factors influencing the outcome of the process include the pressure and flow rate of the gas, the design of the atomizing nozzle, and the composition of the alloy being processed. The gas pressure, for instance, controls the droplet size and the overall powder size distribution, while the choice of gas is crucial to avoid oxidation and contamination of the material. Gas atomization is particularly advantageous due to its ability to produce powders with high purity and a narrow size distribution, which are ideal for use in applications like powder metallurgy, additive manufacturing, and coating technologies [23]. However, the process does have challenges, such as high equipment costs, potential oxidation of reactive alloys, and significant energy consumption, which must be carefully managed to optimize the production of high-quality metallic glass powders.

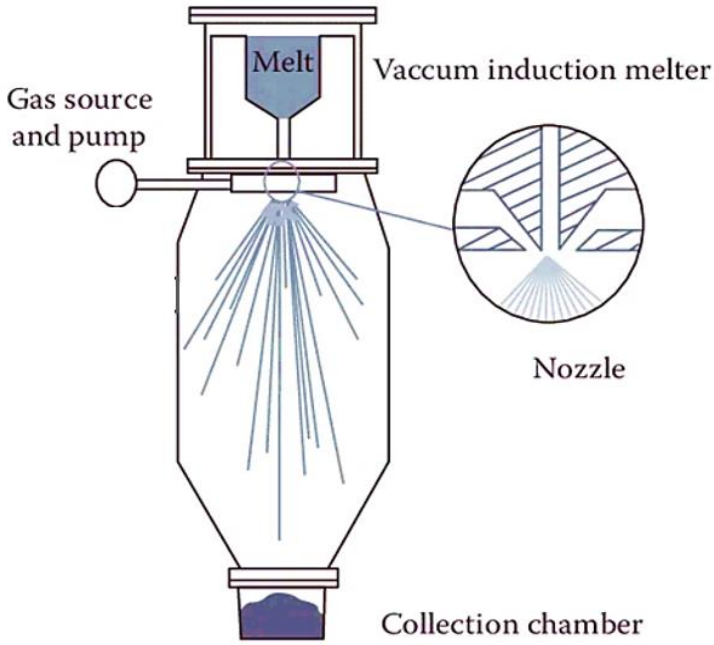

Figure 2.2: Schematic diagram of Gas Atomization process [49].

2.5.1.2. Water Atomization

Water atomization is a widely used method for producing metallic powders, including metallic glass powders, by rapidly cooling molten metal through the interaction with high-pressure water jets. In this process, molten metal is poured or ejected from a nozzle into a chamber where it is directed into a fine spray by a stream of high-pressure water. The water cools and solidifies the molten metal droplets almost instantaneously, resulting in fine particles that are collected at the bottom of the atomization chamber as shown in Figure 2.2. The cooling rate achieved in water atomization, while rapid, is typically slower than in gas atomization, making it more suitable for alloys with lower glass-forming ability (GFA). As the molten droplets interact with water, they break into smaller particles, and the rapid solidification helps to preserve the structure of the alloy. The particle size distribution depends on several factors, such as the nozzle design, water pressure, and the flow rate of the molten metal. Water atomization is often fevered for its cost-effectiveness, especially for large-scale production, compared to gas atomization, which requires more expensive inert gases. However, one of the limitations of water atomization is the potential for oxidation, especially when dealing with reactive metals or alloys that are prone to environmental contamination. To mitigate oxidation, additional protective measures like using controlled atmospheres or post-processing techniques are sometimes necessary. Despite these challenges, water atomization is commonly used for producing metallic powders in powder metallurgy, additive manufacturing, and coating applications, especially for non-glassy alloys or when cost-efficiency is a priority [5].

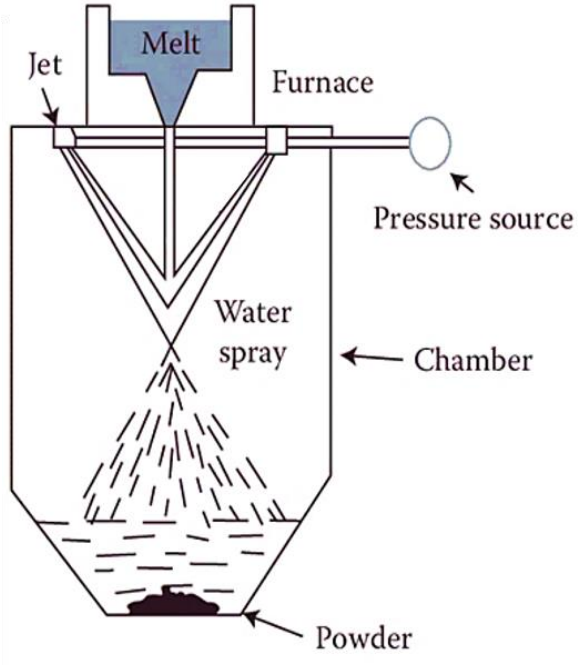

Figure 2.3: Schematic diagram of Water Atomization process [49].

2.5.2. Coating Manufacturing

2.5.2.1. Atmospheric Plasma Spraying

Atmospheric Plasma Spraying (APS) has proven to be a flexible and effective technique for applying high-performance coatings across various industrial applications. Recent

progress has focused on innovative materials and improved equipment to boost properties like thermal, wear, and corrosion resistance.

APS functions by harnessing a high-velocity plasma jet that melts and applies coating materials to surfaces, initiated by the ionization of gases like argon or nitrogen through electrical arcs or high-frequency electromagnetic energy within a specialized plasma torch, which is vital for producing the plasma jet that liquefies the coating particles; these molten particles are then propelled toward the substrate where they impact to create a coating(as shown in Figure 2.3), with the optimization of factors such as plasma power and gas flow rates being critical for achieving the desired coating properties, along with the careful selection of either metal or ceramic materials that significantly affects the coating's performance and traits, thereby demonstrating the integration of cutting-edge technology and material science in delivering high-quality coatings for multiple applications [5].

The behaviour and formation of plasma during spraying processes are shaped by several key elements, including the necessity of electrical discharge for ionizing gases and establishing a conductive energy pathway, the influence of gas flow dynamics like flow rate, pressure, and temperature on plasma stability, the effects of power supply characteristics such as voltage and current on plasma behavior, the importance of plasma torch design including geometry and cooling systems for optimal conditions, and the critical impact of spray distance and angle on plasma-substrate interactions and coating quality, all of which together create a complex framework that dictates the success of plasma spraying operations.

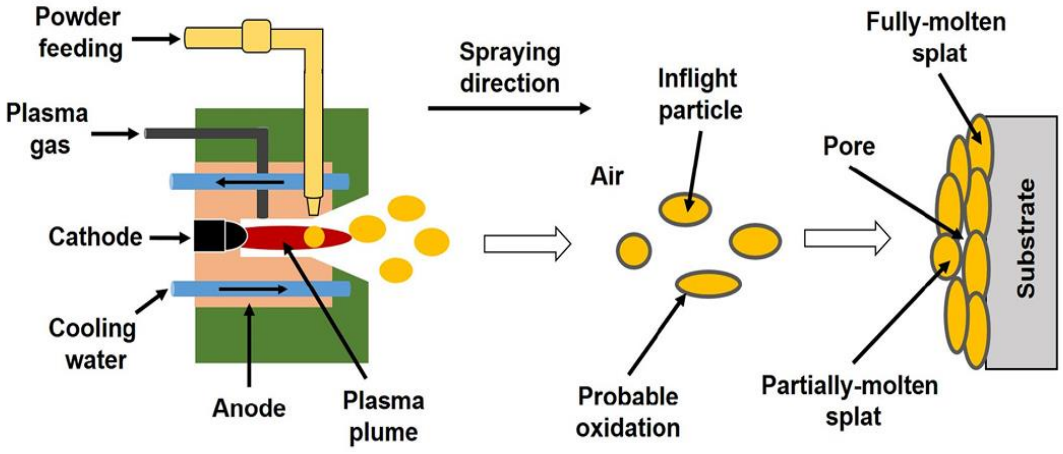

Figure 2.4: Schematic diagram of Atmospheric Plasma Spraying process [12].

In plasma spraying, plasma power plays a critical role in determining the quality and properties of the resulting coating. As the plasma power increases, the energy transferred to the feedstock particles also rises, which improves their melting behavior [51-52]. This results in better adhesion between splats, higher coating density, and reduced porosity. Higher plasma power also enables the deposition of thicker and more uniform layers. However, excessive power can lead to undesirable effects such as evaporation of volatile elements, oxidation, or thermal degradation of sensitive materials. Conversely, if the plasma power is too low, the particles may not fully melt, leading to poor bonding and

weak mechanical properties in the coating. Therefore, optimizing plasma power is essential to achieving coatings with desirable microstructural characteristics, mechanical strength, and corrosion resistance. The ideal power level depends on several factors, including the material being sprayed, substrate properties, and the desired coating performance [51-52].

2.5.3. Ribbon Manufacturing

2.5.3.1. Melt Spun

In melt spinning, a liquid metal jet contacts a rapidly spinning chill wheel (usually copper), extracting heat so quickly that very thin ribbons solidify in the amorphous stat. As Kramer et al. note, most known metallic-glass alloys require such rapid solidification processing (RSP) to avoid the thermally activated formation of crystals [3]. The process produces two cooling stages an initial wheel-contact quench by conduction, followed by a free-flight stage cooled by radiation and convection but in practice the highest cooling occurs during wheel contact, owing to the high thermal conductivity of the copper wheel. The critical cooling rate for glass formation depends on alloy chemistry (glass-forming ability, GFA) and thickness. Bulk metallic glasses (millimetres thick) require exceptionally low critical rates, but thin ribbons can vitrify at ~10^5–10^6 K/s. For example, Wang et al. show that increasing wheel speed from 9 to 30.5 m/s for $Fe_{40}Ni_{40}P_{14}B_6$ alloy raised cooling rates from ~4×10^4 to 6.9×10^6 K/s, with ribbon thickness falling from 92 to 18 μm [4-6]. In general, thinner ribbons (tens of micrometres) cool much faster than thicker strips, so melt spinning inherently yields extremely fine, highly-quenched structures. Many Fe glass ribbons are further annealed to produce fine (≈10–20 nm) nanocrystals within the amorphous matrix, enhancing permeability. Because these glasses contain high iron content and expensive elements like Cu/Nb only in trace, they must be made extremely thin – hence the universal use of melt spinning. As Tiberto et al. note, melt-spun remains the main technique for obtaining amorphous soft-magnetic ribbons of Fe-based alloys [4]. The typical melt-spinner consists of an induction-heated crucible (often quartz or alumina) and a rapidly rotating chilled wheel (usually copper). A small charge (5–100 g) of alloy is melted by induction under vacuum or inert gas [1-2]. The crucible is often made of dense alumina or quartz glass (resistant to heat shock). A pressurized inert gas (Ar or He, 5–70 kPa) propels the melt through a fine nozzle in the crucible bottom, forming a liquid jet or puddle on the wheel as shown in Figure 2.4.

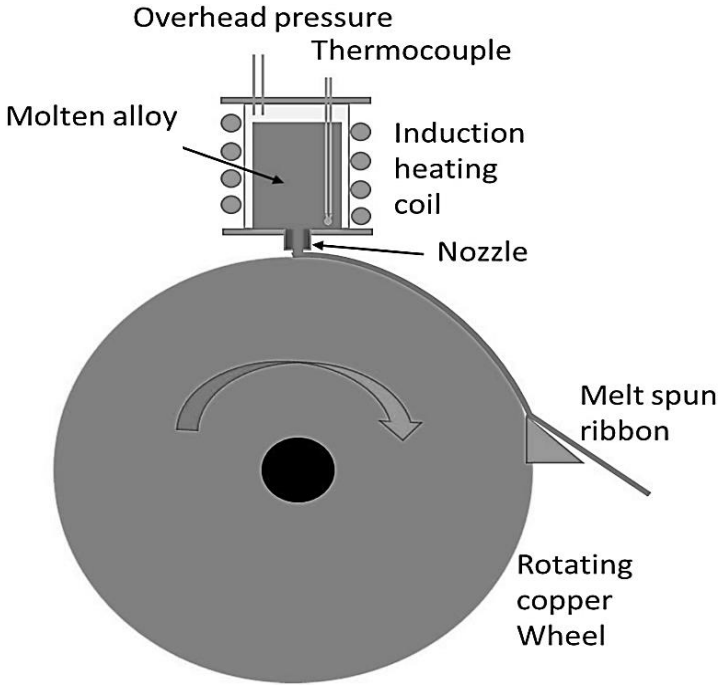

Figure 2.5: Schematic diagram of Melt spun process [50].

- **Wheel:** Water-cooled copper wheel (diameter ~150–300 mm) rotating at high speed. Surface (tangential) speeds are typically 10–50 m/s[3]. (Copper is preferred for its high thermal conductivity; steel or Ni alloys have also been used, but give lower cooling.). Higher wheel speed thins the ribbon and increases quench rate.
- **Crucible & Nozzle:** Crucible material is chosen for chemical compatibility (e.g. quartz or BN). Nozzle orifice is circular (or a slit for planar flow), typically 50–500 μm in. For instance, nozzles from 50 to 1250 μm are reported. Finer orifices and small wheel/nozzle gaps favor thinner ribbons [1-3].
- **Gas Pressure & Atmosphere:** Inert gas (often Ar) at ~10–70 kPa pressure drives the flow [4-5]. Elevated pressure improves wetting between the melt and wheel, enhancing thermal contact. Systems operate under vacuum backfill or controlled atmosphere to prevent oxidation.
- **Ribbon:** Typically, 10–50 μm for high-speed melt spun. As seen in practice, increasing wheel speed from ~9 to 30 m/s shrank FeNiP ribbons from ~92 to 18 μm [3-4]. Industry often targets ~20–30 μm for Fe-glass ribbons (e.g., 15–35 μm at 47 m/s). Thickness is adjusted via wheel speed, melt pressure, and nozzle gap [6].
- **Cooling Rate:** The ribbon cools at ~10^5–10^6 K/s. Melt spinning achieves the extreme quench needed for glass formation. Heat extraction occurs very quickly (within microseconds) as the ribbon contacts the wheel, then slows after detachment [5-6].

2.6. Application of Fe-based MG

Fe-based metallic glasses have found practical applications in a variety of real-life settings, primarily as protective coatings in industries where corrosion, wear, and mechanical fatigue are significant concerns. One of the most prominent applications is in the marine and offshore sector, where these materials are used as coatings on ship components, risers,

propeller shafts, and subsea equipment. For example, Fe-based metallic glass coatings have been applied to steel surfaces exposed to seawater and aggressive salt-spray environments to prevent pitting corrosion and extend service life. These coatings are particularly valuable for turbine blades and pump impellers operating in submerged or splash zones, where traditional stainless steels degrade more quickly. In the renewable energy sector, especially in tidal and wave energy devices, Fe-based glass coatings are used to protect moving components against cavitation erosion and corrosion. Their high hardness and ability to maintain structural integrity under fluctuating loads make them ideal for such dynamic environments.

Beyond marine applications, Fe-based metallic glasses are also employed in soft magnetic applications such as transformer cores and magnetic sensors, where their low coercivity and high saturation magnetization help improve energy efficiency. Nishiyama et al. successfully fabricated bulk metallic glass (BMG) plates with dimensions of 30×20×1 mm using a squeeze casting method, which combines aspects of both casting and forging with $Fe_{73}Ga_4P_{11}C_5B_4Si_3$ alloy composition. This material demonstrated outstanding soft magnetic characteristics, including a saturation magnetization (Is) of 1.32 Tesla, a maximum magnetic permeability (μ_{max}) of 110,000, and a coercivity (Hc) of 33 A/m. After undergoing annealing treatment, the magnetic performance was further enhanced, with μ_{max} increasing to 160,000 and Hc significantly reduced to 2.7 A/m [5]. Utilizing this alloy, the researchers developed a yoke and a prototype linear actuator, showcasing the practical applicability of Fe-based BMGs in magnetic device engineering shown in Figure 2.5(a). In industrial wear components, such as dies, bearings, and cutting tools, Fe-based glass coatings reduce friction and wear under high-load operations. These applications benefit from the material's uniform amorphous structure, which prevents crack initiation and enhances longevity [5]. In real-life applications of Fe-based metallic glasses span from marine coatings and energy systems to electronics and industrial tooling, taking advantage of their combined properties of corrosion resistance, mechanical strength, and magnetic performance. Their growing use in such applications highlights their transition from laboratory research materials to viable solutions in demanding operational environments.

Figure 2.5(b) displays the external appearance and surface quality of commercial $Fe_{44}Co_5Ni_{24}Mo_2B_{17}Si_8$ glassy alloy shots, each about 80 μm in diameter. These were produced using water atomization and subsequently sieved to achieve the desired particle size distribution [25]. The shot peening effectiveness of this alloy was evaluated against two conventional crystalline steels: a high-speed steel composed of Fe–1.15C–4Cr–5Mo–2.5V–6.5W–8Co (wt.%) and a cast steel with Fe–1C–0.9Si–0.7Mn (wt.%). Across all criteria, the Fe-based BMG shots demonstrated superior performance compared to both crystalline counterparts [5].

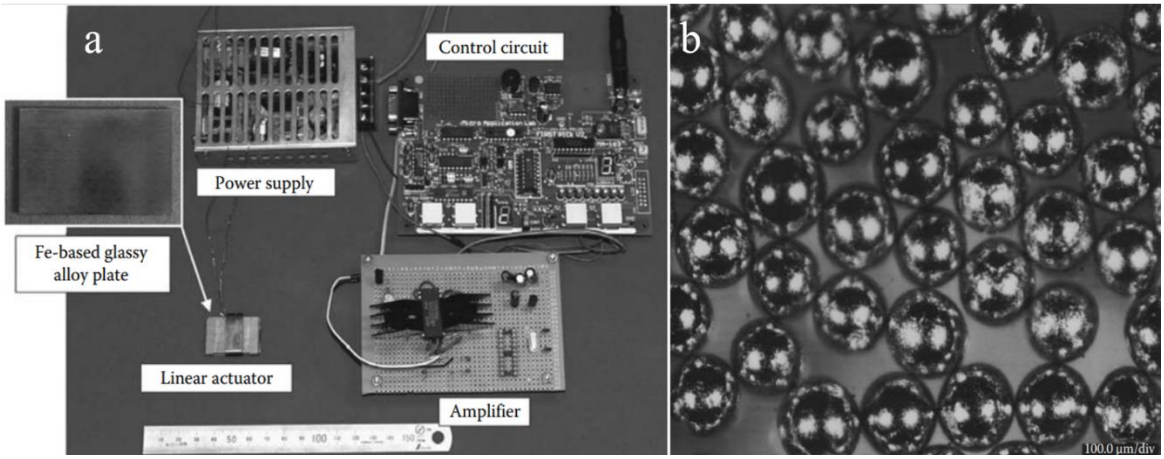

Figure 2.6: (a) A magnetic yoke fabricated using an $Fe_{73}Ga_4P_{11}C_5B_4Si_3$ bulk metallic glass plate for use in a prototype linear actuator. and (b) Shot Peening Balls.

2.7. Corrosion Behaviour of Fe-based MG

Fe-based metallic glasses (MGs) exhibit exceptional corrosion resistance due to their unique disordered atomic structure and high chemical homogeneity. Unlike their crystalline counterparts, metallic glasses lack grain boundaries, phase segregations, and other microstructural defects that typically serve as initiation sites for corrosion [36,40]. The homogeneity eliminates preferred anodic sites, leading to a uniform dissolution mechanism and enhanced passivation. The passivation behaviour in chloride-containing media has been a major focus in Fe-based MG research [46].

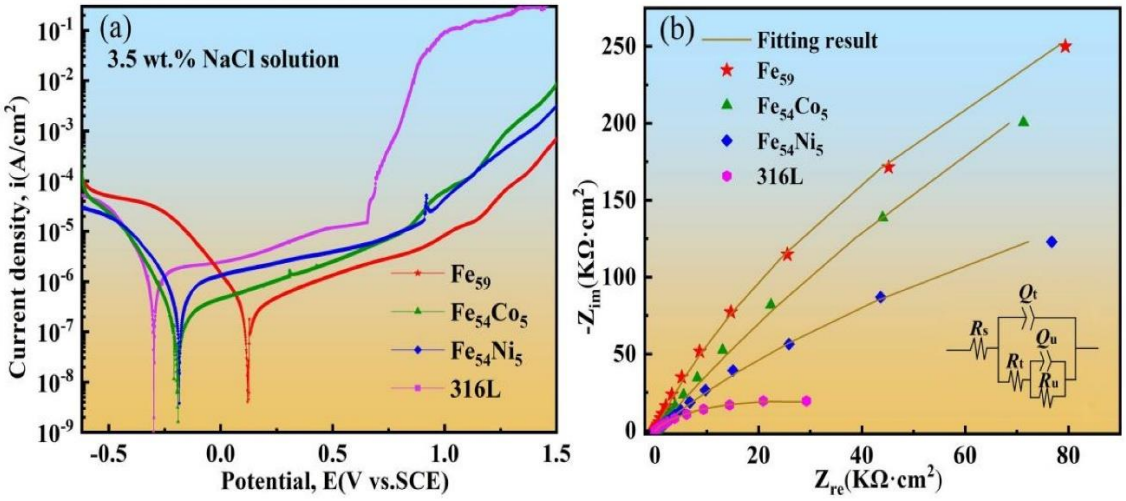

Figure 2.7: (**a**) Potentiodynamic polarization curves in 3.5 wt% NaCl solution at room temperature for $Fe_{54}M_5Cr_{15}Mo_6Si_2B_4P_{10}C_4$ glassy alloy rods and 316L stainless steel; (**b**) Nyquist plots $Fe_{54}M_5Cr_{15}Mo_6Si_2B_4P_{10}C_4$ glassy alloy rods and 316L in 3.5 wt.% NaCl solution at room temperature [21].

The superior corrosion resistance of Fe-based MGs is largely attributed to the spontaneous formation of a stable, protective passive film, primarily composed of oxides and hydroxides of iron and alloying elements such as chromium, molybdenum, or boron [43-45]. This passive layer effectively suppresses anodic dissolution and retards the diffusion

of aggressive ions like Cl^-, which are known to accelerate localized corrosion processes in conventional steels [42]. Electrochemical and X-ray photoelectron spectroscopy (XPS) studies reveal that the passive films predominantly consist of Fe_2O_3, Cr_2O_3, B_2O_3, and MoO_3, forming a complex, self-healing oxide layer [38]. Cr promotes the formation of a dense, adherent Cr_2O_3 layer, which increases pitting resistance [39]; on the other hand, Mo contributes to passivation kinetics by forming soluble MoO_4^{2-}, aiding in film self-repair [40]. Moreover, boron and phosphorus, often included for glass-forming ability, are oxidized to B_2O_3 and PO_4^{3-}, which also stabilize the passive film and mitigate Cl^- attack [41]. The corrosion process in metallic glasses is controlled by a homogeneous surface reaction, ensuring uniform degradation rather than localized attacks such as pitting or intergranular corrosion. Studies have shown that the passivation behavior is greatly influenced by the alloy composition and the pH of the corrosive environment [48]. For example, Fe-Si-B metallic glasses demonstrate excellent passivity in both acidic and neutral chloride-containing solutions, maintaining low passive current densities and minimal weight loss [47].

Electrochemical impedance spectroscopy (EIS) studies often model the passive film as a two-layer structure (inner compact oxide + outer porous oxide). The high charge transfer resistance and low capacitance confirm a dense, protective barrier [43]. Zang G. et al. conducted a study in which electrochemical and electrochemical impedance spectroscopy (EIS) analyses were performed to evaluate the corrosion behavior of Fe-based bulk metallic glasses (BMGs) in a 3.5% NaCl solution, as shown in Figure 2.5. The results revealed that these BMGs demonstrated significantly improved corrosion resistance when compared to 316L stainless steel. Notably, their corrosion current densities (Icorr) were remarkably low, ranging between 10^{-8}-10^{-7} A/cm² as shown in Table 2.2. Among the tested compositions, the Fe_{59} BMG stood out, displaying the most positive corrosion potential (Ecorr), the lowest corrosion current, and a broad, highly stable passive region, indicating its superior corrosion resistance [21].

Table 2.2: Electrochemical parameters derived from potentiodynamic polarization curves [21].

Alloys	E_{corr} (V)	I_{corr} ($\times 10^{-8}$ A·cm^{-2})
$Fe_{59}Cr_{15}Mo_6Si_2B_4P_{10}C_4$	−0.12	8.4
$Fe_{54}Co_5Cr_{15}Mo_6Si_2B_4P_{10}C_4$	−0.19	8.6
$Fe_{54}Ni_5Cr_{15}Mo_6Si_2B_4P_{10}C_4$	−0.18	38.3
316L	−0.29	98.5

Just by the addition of 0–4 at.% Cr in an alloy of Fe-based metallic glass drops from 700 to 1.6 μm/year corrosion rate was seen [5]. Mo additions can enhance corrosion resistance only in moderation; excessive amounts lower the stability of the passive film. B and Nb play synergistic roles in increasing corrosion resistance, with Nb aiding in the formation of passive films rich in refractory elements. Further increasing B from 4% to 8% in $Fe_{50-x}Cr_{16}Mo_{16}C_{18}B_x$ alloy reduces the corrosion rate significantly. Rare earth elements like Yttrium (Y), when added in small amounts in combination with other elements like Cr and Mo, can refine the structure and enhance corrosion resistance. Table 2.3 shows the effect of alloying elements on the corrosion resistance property of MG.

Table 2.3: Effect of alloying elements on the Corrosion Resistance property [5].

Alloying Element	Effect on Corrosion Resistance
Chromium (Cr)	Enhances corrosion resistance by forming a stable passive film.
Boron (B)	Improves corrosion resistance by refining the microstructure and enhancing the passive layer.
Phosphorus (P)	Enhances glass-forming ability and stabilizes passive film, leading to better corrosion resistance.
Carbon (C)	Acts as a glass former and refines microstructure, indirectly contributing to corrosion resistance.
Silicon (Si)	Enhances passivation, especially in chloride-containing environments; contributes to improved corrosion resistance.

2.8. Material selection

In this work, Fe-based metallic glass systems, specifically **$Fe_{73}Cr_2Si_{11}B_{11}C_3$** and **$Fe_{80}Cr_{10}B_4C_2P_4$,** were selected to develop protective coatings for harsh marine and industrial environments. These alloys were chosen due to their well-documented amorphous-forming ability, high corrosion resistance, and superior mechanical properties, including elevated hardness and excellent wear resistance. The inclusion of Cr enhances passivation and stability of the protective oxide layer in chloride-containing solutions, which is critical for long-term durability in seawater [21-25]. Si, B, C, and P contribute to glass formation and mechanical reinforcement, while maintaining thermal stability and resisting crystallization during deposition processes such as atmospheric plasma spraying (APS). Among several candidate systems (including conventional stainless steels and other metallic glasses), these Fe-based compositions offer a favourable balance of cost-effectiveness, amorphous structure retention, and application-specific performance. Their proven performance in saline corrosion testing and compatibility with scalable coating technologies make them suitable for applications such as offshore structures, pumps, turbine blades, and ship components exposed to aggressive marine conditions.

CHAPTER 3

3. Experimental Procedure

3.1. Synthesis of Metallic Glasses Coatings and Ribbons

Fe-based fully amorphous powder with compositions **$Fe_{73}Cr_2Si_{11}B_{11}C_3$** (at.%) were produced via gas atomization and used to fabricate coatings on mild steel substrates (dimensions: 100 mm × 100 mm × 2 mm). The deposition process was carried out using a Plasma torch (Metallizing Equipment Company Pvt. Ltd., India), applying the atmospheric plasma spraying technique under the conditions specified in Table 3.1. A total of four coated samples were prepared: three coatings (Coating 1, 2, and 3) used the same alloy composition but varied spray parameters to allow for comparative evaluation, while Coating 4 was applied using the alternate alloy composition, as **$Fe_{80}Cr_{10}B_4C_2P_4$** (at.%). Additionally, melt-spun ribbons with the **$Fe_{80}Cr_{10}B_4C_2P_4$** composition were produced using a melt-spun setup under an argon atmosphere, with operational parameters detailed in Table 3.2. For electrochemical analysis, standardized specimens measuring 1 cm × 1 cm were sectioned from the coated samples, and all tests were conducted on these prepared specimens under controlled conditions.

Table 3.1: Factors utilized for applying Fe-based nanocrystalline/ amorphous coatings through Atmospheric Plasma Spraying (APS)

	Coating 1	**Coating 2**	**Coating 3**	**Coating 4**
Powder feed rate	40 g/min	40 g/min	40 g/min	40 g/min
Plasma Power	25 kW	30 kW	35 kW	30 kW
Composition (at. %)	$Fe_{73}Cr_2Si_{11}B_{11}C_3$			$Fe_{80}Cr_{10}B_4C_2P_4$
Coating Thickness	~ 100 ± 20 μm			

Table 3.2: Factors utilized for manufacturing Fe-based ribbon through melt spun

	Ribbon 1	**Ribbon 2**	**Ribbon 3**
Wheel Speed	1700 rpm	2100 rpm	3000 rpm
Composition (at. %)	$Fe_{80}Cr_{10}B_4C_2P_4$		

3.2. Characterization Techniques Methods

The microstructural characterization of both the feedstock powders and the resulting coatings was carried out using a high-resolution scanning electron microscope (SEM, SUPRA 40, Carl Zeiss AG, Germany). This instrument, known for its exceptional resolution and extensive depth of field, enabled detailed observation of surface morphology and structural features. For the purpose of porosity analysis, SEM images were captured from the polished top surface of the coatings at a magnification of 500×, providing sufficient clarity for quantitative and qualitative evaluation of porosity distribution and morphology. To determine the phase composition of the as-sprayed

coatings as well as the initial powders, X-ray diffraction (XRD) analysis was conducted using a Rigaku SmartLab diffractometer (Japan) equipped with Cu-Kα radiation. The scans were performed over a 2θ angular range of 30° to 110°, allowing identification of crystalline phases or confirmation of the amorphous nature of the material.

3.3. Electrochemical Testing

To evaluate the corrosion resistance of the as-sprayed Fe-based metallic glass coatings, electrochemical analysis was carried out using a 3.5 wt.% NaCl aqueous solution, which serves as a representative electrolyte for simulating marine and chloride-rich environments. This testing aimed to assess the protective behavior of the coatings under aggressive ionic exposure and to characterize their electrochemical stability. This testing was employed on Gamry Instruments – Interface 1010 E equipment (Figure 3.1).

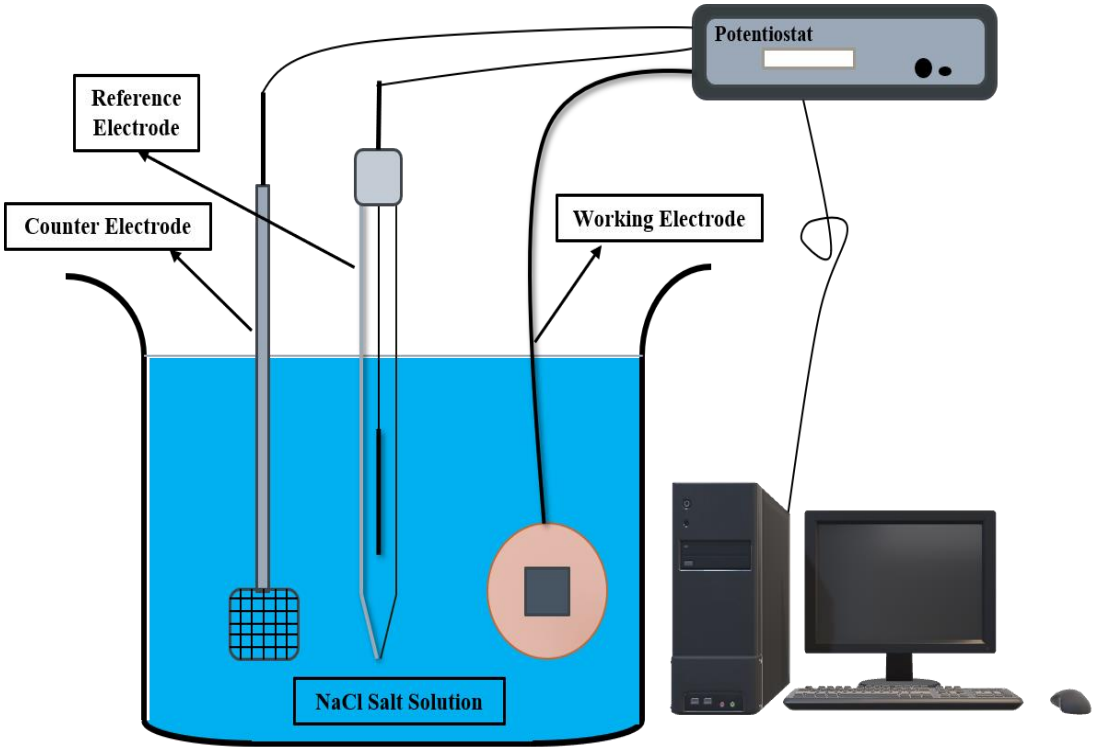

Figure 3.1: Electrochemical Testing Equipment.

3.3.1. Electrochemical Impedance Spectroscopy (EIS)

Electrochemical Impedance Spectroscopy (EIS) was conducted to provide deeper insight into the electrochemical characteristics and corrosion protection performance of the Fe-based metallic glass coatings. EIS is a powerful non-destructive technique that enables the evaluation of interfacial properties, including charge transfer resistance, capacitance, and the nature of the passive film formed on the coating surface. The measurements were performed using a typical three-electrode electrochemical setup. The impedance data were collected by applying a sinusoidal AC voltage of 10 mV (rms) amplitude across a frequency range spanning from 100 kHz to

0.01 Hz. The frequency sweep included 10 data points per decade, which ensured high-resolution characterization of both high- and low-frequency responses. This wide frequency range enabled analysis of both solution resistance and diffusion-controlled processes, as well as the behavior of any protective oxide layers formed on the coating surface.The acquired impedance spectra were represented in both Nyquist and Bode plots, which were subsequently interpreted using equivalent electrical circuit models.

3.3.2. Potentiodynamic Polarization (PDP)

To further investigate the corrosion behaviour of the Fe-based metallic glass coatings, potentiodynamic polarization tests were performed. This method provides insight into the kinetics of electrochemical reactions occurring at the coating surface and is essential for quantifying parameters such as corrosion potential (E_corr) and corrosion current density (i_corr).The polarization experiments were conducted using a standard three-electrode electrochemical cell. The coated specimen served as the working electrode, while a Silver/Silver chloride (Ag/AgCl) was employed as the reference and a platinum mesh electrode was employed as counter electrodes, respectively. Prior to testing, the working electrode was stabilized in the electrolyte under open circuit potential (OCP) conditions for approximately 60 minutes to establish a steady electrochemical state. The resulting polarization curves were recorded and analysed to determine the passivation behaviour, pitting susceptibility, and overall corrosion resistance of the coatings.

Data obtained from the Tafel region of the polarization curves were extrapolated to estimate the corrosion current density (icorr) using standard electrochemical software. Lower icorr values are indicative of reduced corrosion activity and better protective characteristics of the coating. The shape of the polarization curves also helped distinguish between active, passive, and trans-passive regions, providing a more comprehensive view of the coating's behaviour in the chloride-rich environment.

3.3.3. Surface Characterization Post-Polarization

Following electrochemical testing, surface characterization of the corroded coatings was conducted to determine the nature and distribution of the corrosion products formed during the potentiodynamic polarization process. Raman spectroscopy was utilized for this purpose, offering molecular-level insight into the oxidation states and chemical species present on the exposed surfaces. The analysis was carried out using a Raman spectrometer (Model S52L, Nost. Co. Ltd., Korea) equipped with a Cobalt laser at 532 nm excitation wavelength, operating across a detection range of 200–1400 nm. This enabled the identification of iron oxides and related corrosion by-products indicative of the coating's electrochemical behaviour.

3.3.4. Surface Morphological Analysis

Complementary to Raman analysis, surface morphology of the post-corrosion specimens was examined using high-resolution imaging to assess the formation of oxides, pitting, or microstructural degradation. These observations provided qualitative evidence of the coating's degradation mechanisms and supported the

electrochemical results, offering a more complete understanding of its corrosion resistance under saline conditions. The potentiodynamic polarization results, when correlated with the EIS and post-corrosion surface analyses, contributed to a thorough assessment of the coatings' performance and their suitability for use in aggressive marine or industrial applications.

CHAPTER 4

4. Results and Discussion

4.1. Phase Analysis and Microstructural Characterization

Figure 1a presents the microstructural features of the gas-atomized powders used in the atmospheric plasma spraying process. The powders exhibit a particle size distribution ranging approximately from 5 μm to 70 μm, with the average particle diameter measured at 25 μm. Morphologically, the particles are predominantly spherical, a characteristic that facilitates uniform flow during the spraying process and contributes to consistent coating quality. The broad particle size distribution is considered advantageous, as it plays a significant role in influencing both the corrosion resistance and mechanical performance of the final coating [28-30] Specifically, the presence of coarser particles within the distribution has been associated with enhanced corrosion resistance and improved retention of the amorphous phase during deposition. This is attributed to their higher thermal inertia, which limits excessive crystallization during rapid cooling [7-9]. On the other hand, finer particles contribute to the formation of dense microstructures, resulting in improved mechanical properties, such as hardness and wear resistance, due to better packing and reduced porosity in the sprayed layer.

To verify the structural nature of the as-atomized powder, X-ray diffraction (XRD) analysis was conducted, and the corresponding pattern is shown in Figure 1b. The XRD spectrum revealed a broad diffuse halo without any sharp Bragg peaks, confirming the fully amorphous nature of the powder. This observation is consistent with the high glass-forming ability (GFA) of the selected alloy system, $Fe_{73}Cr_2Si_{11}B_{11}C_3$ (at.%), which is known to form an amorphous phase readily under rapid solidification conditions typical of gas atomization [12-14].

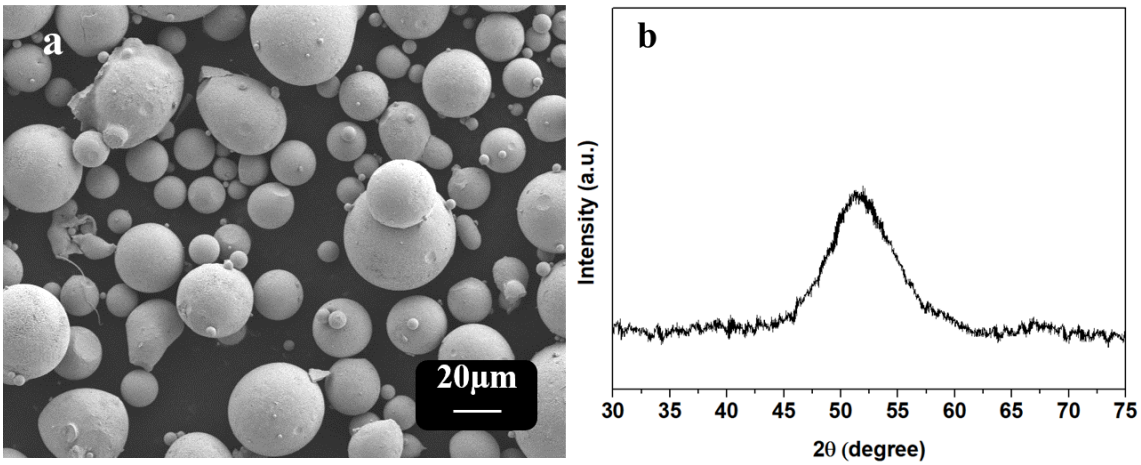

Figure 4.1: (a) SEM image displays Fe-based feedstock powder with a spherical shape, while (b) XRD pattern shows a broad and hollow peak indicative of its amorphous nature.

Figure 2 illustrates the surface morphology and cross-sectional microstructures of the Fe-based metallic glass coatings deposited onto mild steel substrates using atmospheric plasma spraying at varying plasma power levels. The coatings were developed under three different plasma powers 25 kW (Coating 1), 30 kW (Coating 2), 35 kW (Coating 3) and (Coating 4) to investigate the influence of thermal input on coating quality, microstructure, and porosity [12-14].

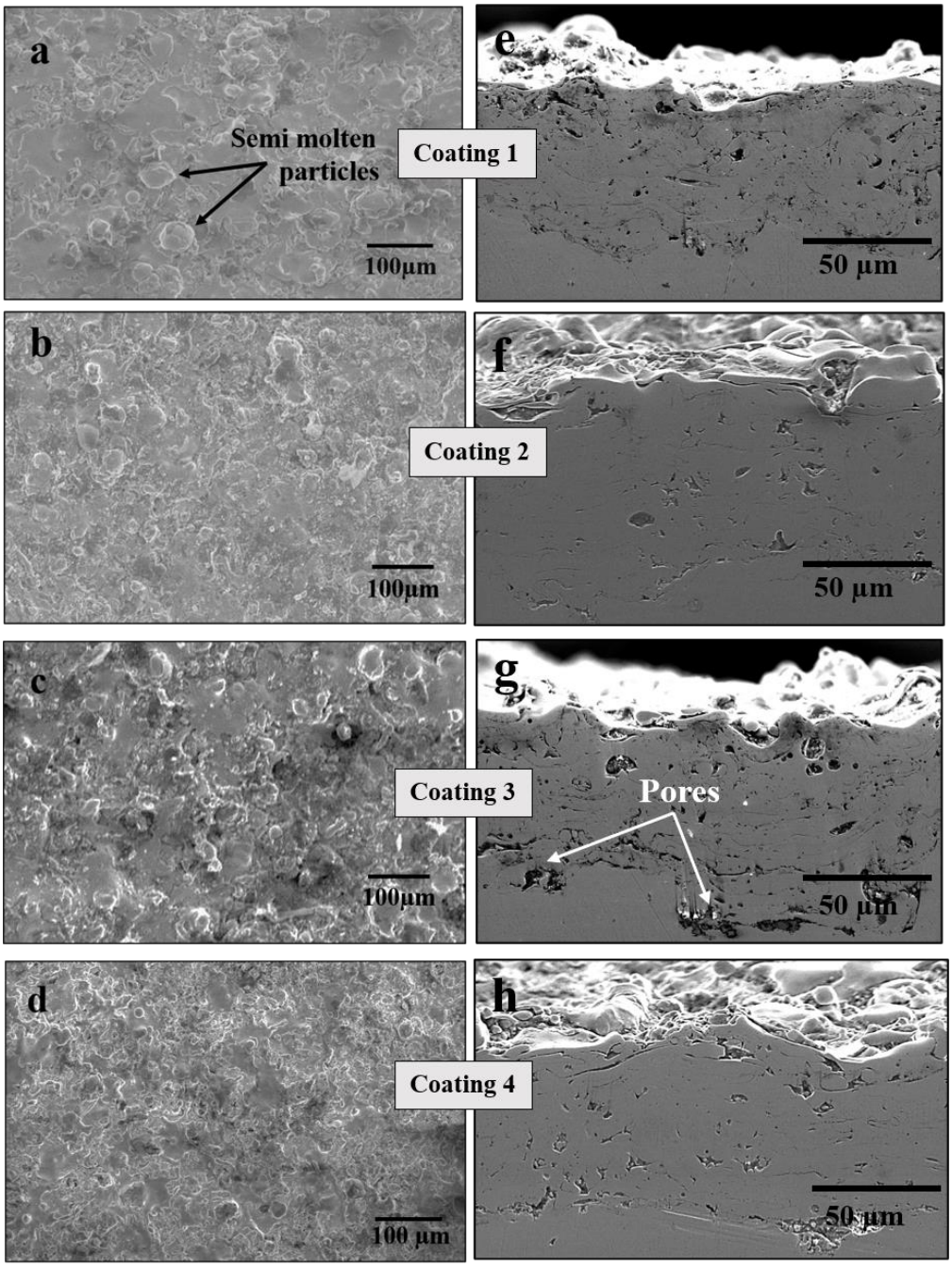

Figure 4.2: SEM images displaying (a-d) top as-sprayed surfaces and (e-h) cross-sectional surfaces of the coatings.

The top-surface SEM image of Coating 1 (Figure 4.2a) reveals a significant proportion of partially molten particles, indicating insufficient melting during the spraying process at the lowest plasma power setting. This incomplete melting often leads to poor particle flattening and weak inter-splat bonding, which adversely affects coating density and integrity. However, as the plasma power increases to 30 kW and 35 kW, the morphology of Coating 2 and Coating 3 (Figure 4.2b and Figure 4.2c) shows a noticeable decrease in the number of partially melted particles [17-18]. In the morphology of Coating 4 (Figure 4.2d), we report the decreased partially melted particles. This enhancement in melting

behavior is attributed to the greater energy input at higher power levels, which improves thermal efficiency, allowing more uniform particle melting and splat formation.
Further insights were obtained from the cross-sectional SEM images of the coatings (Figure 4.2), which clearly demonstrate a reduction in porosity with increasing plasma power. Quantitative analysis of the pore volume fraction revealed that Coating 1 exhibited a porosity level of approximately 10 vol.%, whereas Coating 2, Coating 3 and Coating 4 exhibited reduced porosities of about 8 vol.%, 5 vol.% and 7%,.% and 5 vol.%, respectively. The observed trend can be explained by the enhanced deposition quality at elevated plasma powers: as more fully molten particles impact the substrate and previously deposited layers, they are more capable of filling voids and irregularities, leading to denser coatings. Moreover, the thermal energy accumulated from sequential splat stacking promotes local remelting and bonding, facilitating splat fusion and improving adhesion between layers (12-14).

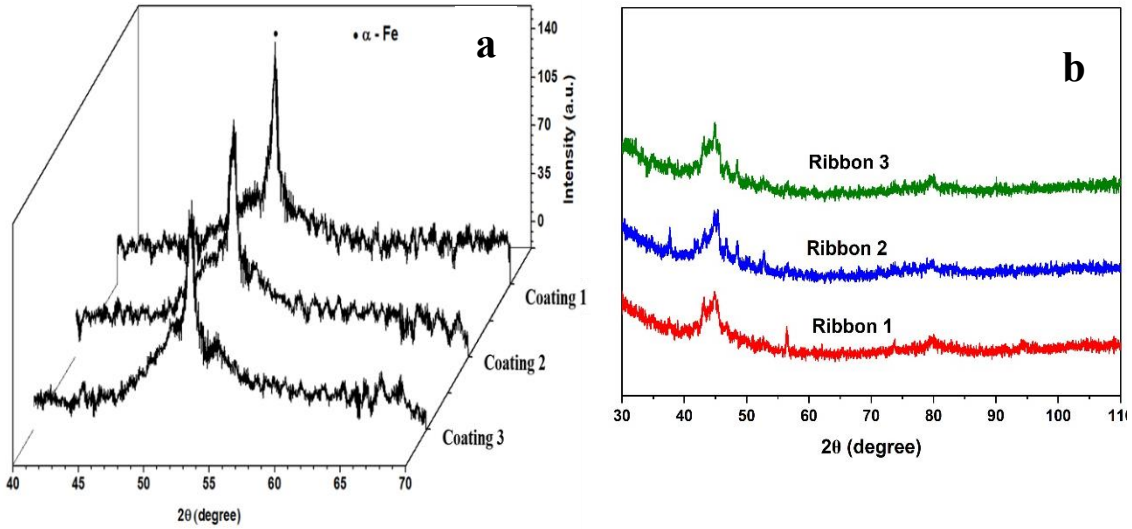

Figure 4.3: XRD patterns of different coatings (a) and Ribbons (b) show differences in their crystallization.

The structural evolution of the coatings was further analyzed using X-ray diffraction (XRD), with the patterns shown in Figure 4.3. The diffraction spectra exhibit a characteristic broad hump in the 2θ range of 45°–60°, indicative of the presence of an amorphous phase, along with a few distinct crystalline peaks identified as α-Fe [16-19]. The degree of amorphousness was found to decrease with increasing plasma power, attributed to the greater heat input and longer thermal exposure, which promote nucleation and growth of crystalline phases. According to the XRD intensity-based estimation method described by Kumar et al. (2019), the amorphous phase content in Coating 1, Coating 2, Coating 3, and Coating 4 was approximately 90%, 84%, 75%, and 86%, respectively. This decreasing trend highlights the trade-off between improved coating density and reduced amorphous phase retention at higher spraying energies [12].
Collectively, these results underscore the critical influence of plasma power on the microstructural features and phase composition of Fe-based metallic glass coatings. Optimizing spray parameters is therefore essential to achieve the desired balance between amorphous structure preservation and mechanical integrity.

4.2. Electrochemical Behaviour

Potentiodynamic polarization experiments were conducted in a 3.5 wt% NaCl solution to systematically characterize the corrosion behavior of the plasma-sprayed coatings. The recorded polarization curves (Figure 4.4) were analyzed to extract the corrosion potential (Ecorr) and corrosion current density (icorr) via Tafel extrapolation. The results summarized in Table 3.1 indicate a pronounced and nonlinear dependence of corrosion performance on the plasma spray power. Specifically, increasing the plasma power from 25 kW to 30 kW caused icorr to decrease from 13.4 $\mu A/cm^{-2}$ to 9.7 $\mu A/cm^{-2}$, signifying a substantial improvement in corrosion resistance at 30 kW. However, a further increase to 35 kW caused icorr to rise to 16.$\mu A/cm^{-2}$, reflecting a deterioration of protective behavior at the highest energy input. Among the samples, Coating 2 (fabricated at 30 kW) exhibited the most noble corrosion potential (approximately –485 mV) and the lowest corrosion current density, indicating superior resistance to localized corrosive attack relative to the others [20-22]. These observations suggest that the intermediate plasma power yields the most effective combination of coating characteristics for corrosion protection.

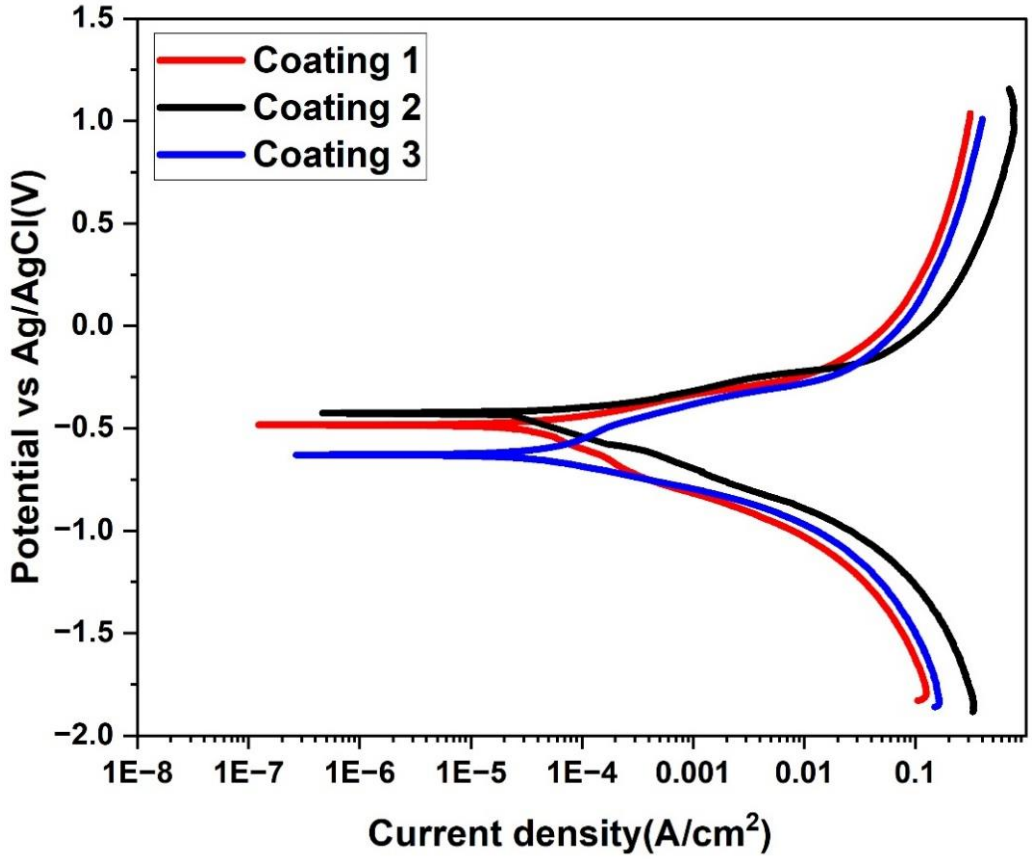

Figure 4.4: Potentiodynamic polarization curves of coated samples.

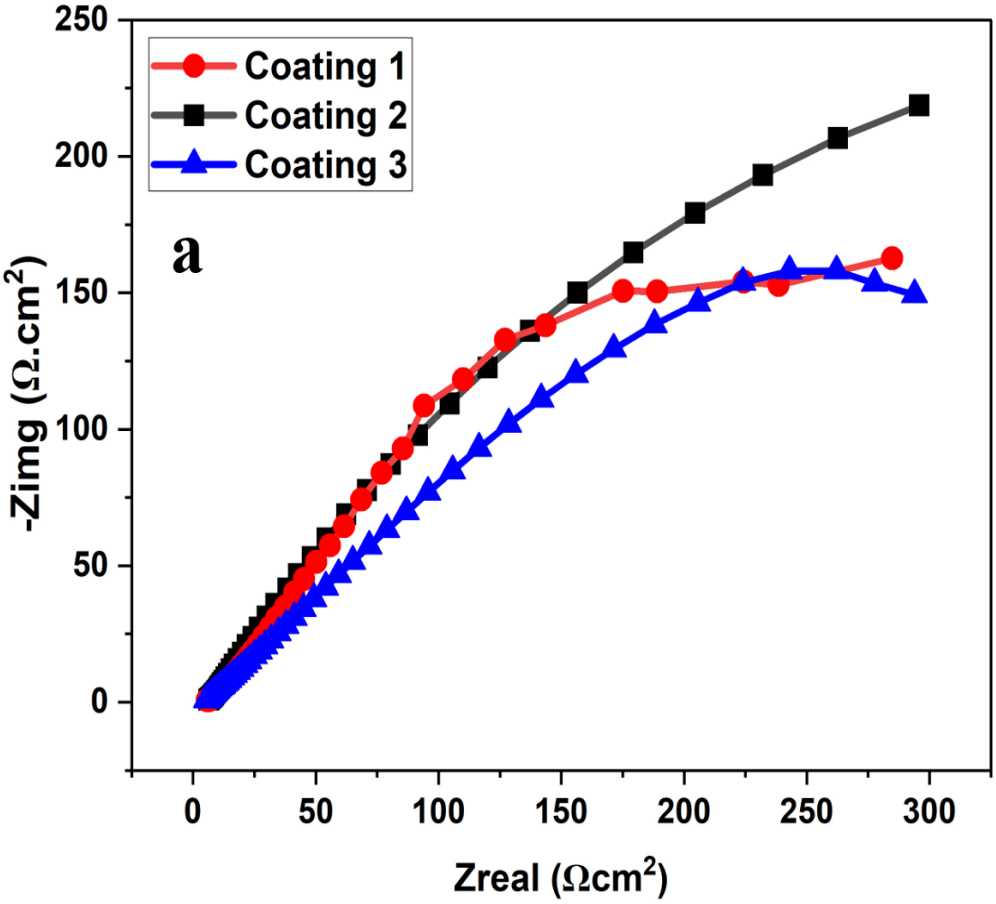
Coating 1
Coating 2
Coating 3
a
-Zimg (Ω.cm²)
Zreal (Ωcm²)
0
50
100
150
200
250
300

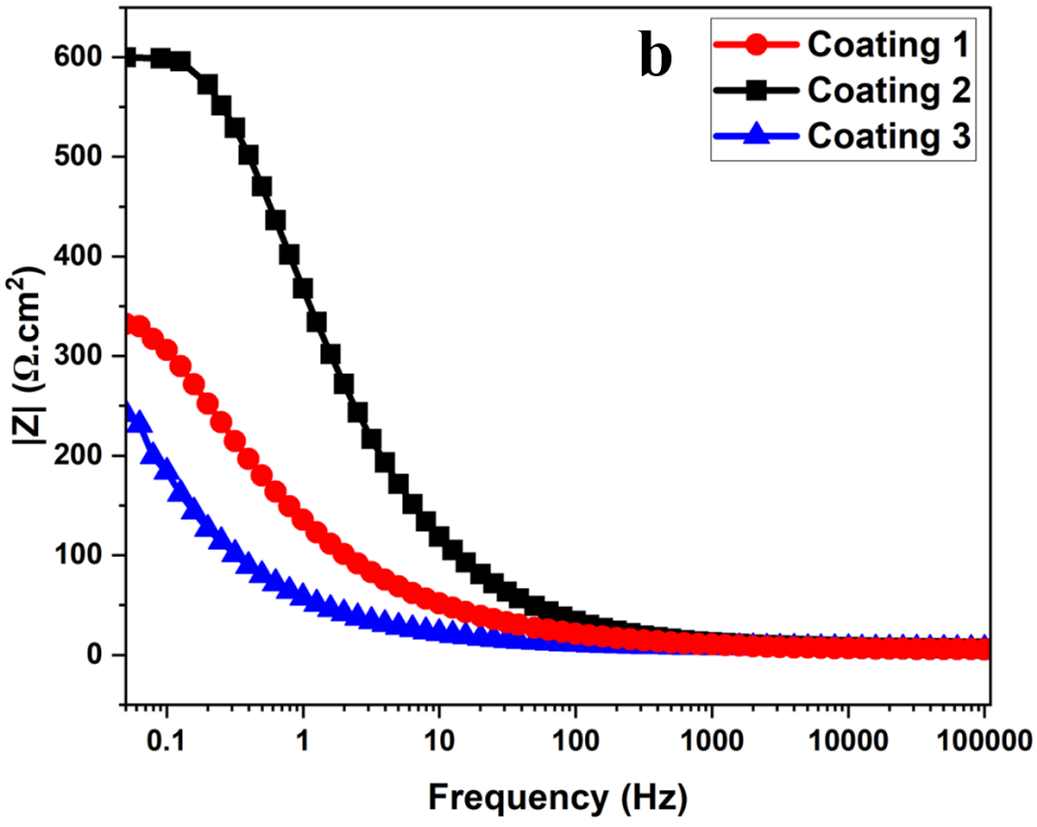
b
Coating 1
Coating 2
Coating 3
|Z| (Ω.cm²)
Frequency (Hz)
0
100
200
300
400
500
600
0.1
1
10
100
1000
10000
100000

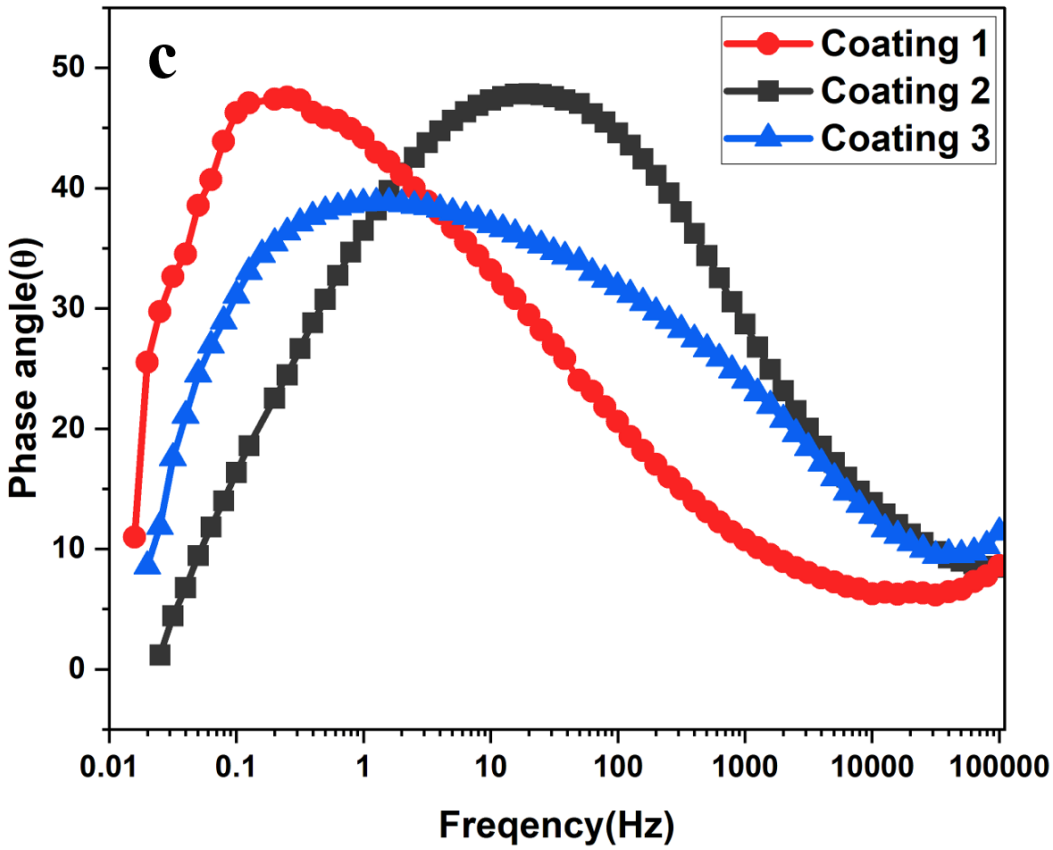

Figure 4.5: Electrochemical impedance plots of coatings deposited at different plasma power and exposed to 3.5% NaCl solution. (a) Nyquist plot, (b) Bode impedance plot, (c) Bode phase angle plot.

Electrochemical impedance spectroscopy (EIS) measurements further corroborate these conclusions. In the Nyquist plots (Figure 4.5a), Coating 2 showed the largest semicircular arc among all samples, corresponding to the highest charge-transfer resistance (R_{ct}) at the metal/coating interface. A larger R_{ct} implies that the passive film is more resistive to ion transport, indicating a more protective barrier against corrosion [5,17,23]. In the Bode magnitude plots (Figure 4.5b), Coating 2 also maintained the highest impedance at low frequencies, reflecting its superior resistive behavior against electrochemical attack. Moreover, the Bode phase-angle plot (Figure 4.5c) for Coating 2 exhibited a broad peak near 48.9°, characteristic of a dominant capacitive response over a wide frequency range. This high, broad phase-angle peak indicates a compact and stable passive layer. Together, the polarization and impedance analyses confirm that their microstructural quality and phase composition strongly govern the corrosion resistance of these coatings. An optimal plasma-spray power (in this case, 30 kW) produces a coating with maximal passive film stability and minimal corrosive current, underscoring the complex interplay between processing parameters and electrochemical performance [9].

Because all coatings were produced from the same feedstock material, bulk chemistry differences are negligible, and the observed performance variations must stem from microstructural and phase differences induced by the deposition parameters [20,24]. At 30 kW, the spray conditions likely promoted optimal particle melting and flattening,

resulting in a relatively dense, homogeneous lamellar structure with minimal porosity. Such a microstructure would impede the ingress of aggressive chloride ions and support the formation of a stable passive oxide film. In contrast, at the highest power (35 kW) excessive thermal input may have introduced higher thermal stresses or partial re-melting of layers, creating microcracks or other defects that compromise the passive layer's integrity. Similarly, the coating produced at 25 kW may contain higher porosity or incomplete particle bonding, which would also weaken its corrosion resistance. Thus, the intermediate-power coating benefits from a microstructure that maximizes barrier properties and minimizes defect-related pathways for corrosion [26-28].

4.3. Raman Analysis

Raman spectroscopy was employed as a complementary analytical technique to characterize the corrosion products formed on the surface of iron-based materials exposed to corrosive environments. This method provided detailed insights into the chemical composition and structural variations of rust layers formed during electrochemical degradation. The spectra obtained, as shown in Figure 4.6, clearly indicated the presence of multiple iron oxide and iron oxyhydroxide phases, notably lepidocrocite (γ-FeOOH), maghemite (γ-Fe_2O_3), and akageneite (β-FeOOH) [12-14].

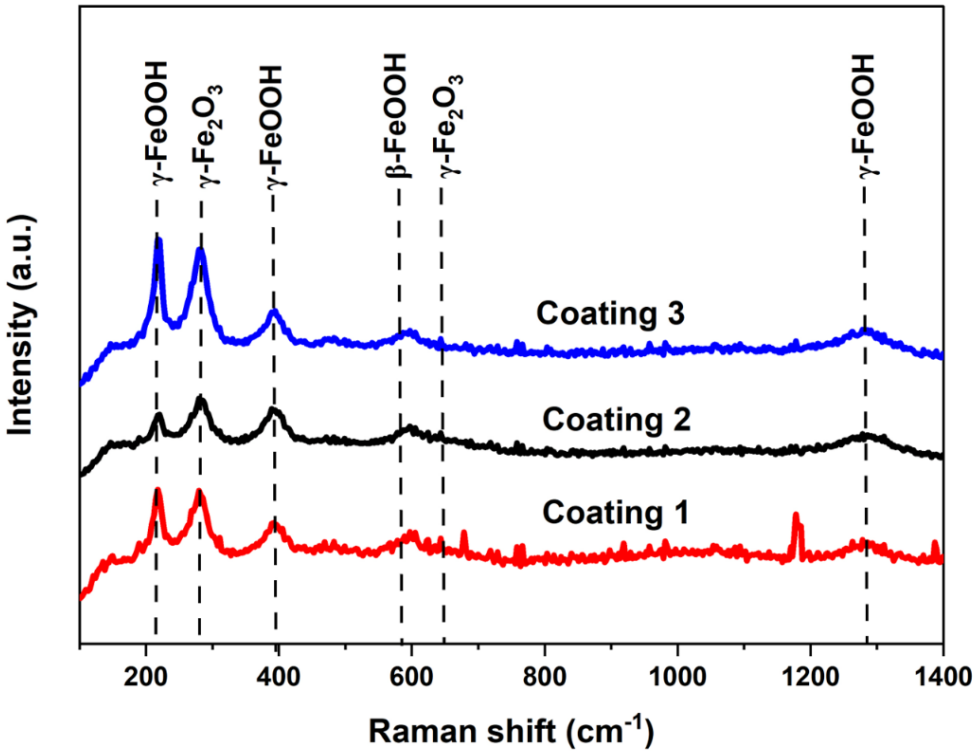

Figure 4.6: Raman spectra of coating displaying characteristic peaks of various oxides and hydroxides phases.

Among these identified phases, maghemite (γ-Fe_2O_3) is generally recognized for its structural stability and inert behavior under a variety of environmental conditions [10]. In

contrast, both lepidocrocite and akageneite are metastable phases that tend to degrade more rapidly, particularly when exposed to saline or chloride-rich environments, which are common in marine or industrial settings. The presence of akageneite, in particular, is often associated with the ingress of chloride ions and is typically formed in highly aggressive corrosion scenarios. Interestingly, despite their known instability, a higher relative content of γ-FeOOH and β-FeOOH phases in the corrosion layer has been linked to improved corrosion resistance in this study. This counterintuitive behavior can be attributed to the formation of a compact and adherent rust layer that acts as a partial barrier against further electrolyte penetration. The fine distribution and compactness of these phases may reduce the diffusion pathways for corrosive species, thereby slowing down the progression of corrosion [17-18].

Overall, the Raman spectroscopy analysis not only confirmed the heterogeneous nature of the rust layers but also highlighted the crucial role that the composition and morphology of these corrosion products play in influencing the protective properties of the passive film [22-24]. This underscores the importance of phase-specific identification of corrosion by-products in understanding the degradation mechanisms of Fe-based metallic glasses and optimizing their corrosion resistance for long-term applications.

4.4. Ribbon Corrosion Study

As shown in Table 3.2, four ribbons with different parameters but similar composition were employed to optimize the processing conditions. Potentiodynamic polarization experiments were conducted in a 3.5 wt% NaCl solution, and the recorded polarization curves (Figure 4.7) were analysed. Further electrochemical impedance spectroscopy (EIS) experiments were performed, yielding Nyquist (Figure 4.8), Bode Impedance (Figure 4.9), and Bode Phase Angle (Figure 4.10) plots, respectively. Ribbon 2 demonstrated the lowest corrosion current density (icorr) of 0.0116 μA cm^{-2} and a comparatively more positive corrosion potential (Ecorr), highlighting its strong passivation capability in a corrosive environment, as illustrated in Figure 4.7. The findings from the potentiodynamic polarization analysis were consistent with the electrochemical impedance spectroscopy (EIS) results. As shown in Figure 4.9, Ribbon 2 maintained the highest impedance values at low frequencies, reinforcing its superior corrosion resistance [14-18]. In the Nyquist plot, the diameter of the semicircle, which represents the material's corrosion protection efficiency, followed the increasing order: Ribbon 1 < Ribbon 3 < Ribbon 2, confirming the excellent barrier properties of Ribbon 2 (Figure 4.8). Additionally, Bode phase angle analysis showed peak values of 40.52° for Ribbon 1, 67.69° for Ribbon 2, and 63.44° for Ribbon 3 (Figure 4.10). The broader phase angle of Ribbon 2 indicates improved protective behavior in corrosive media, suggesting higher chemical stability and a more durable passive film [18].

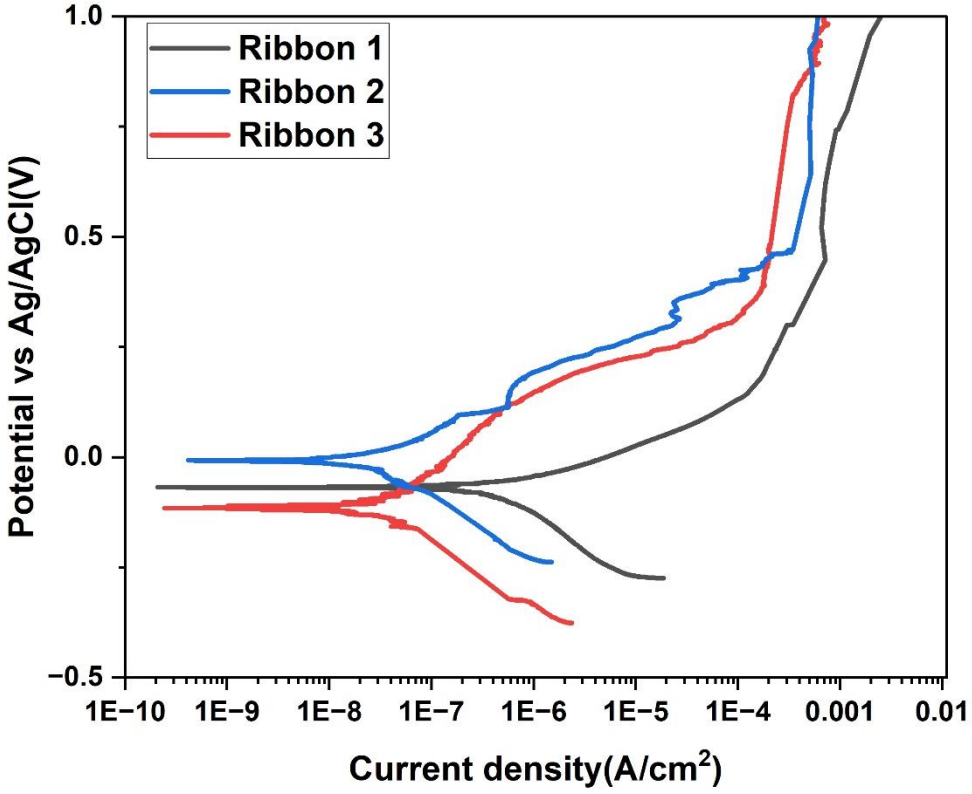

Figure 4.7: Potentiodynamic polarization curves of the Ribbon sample.

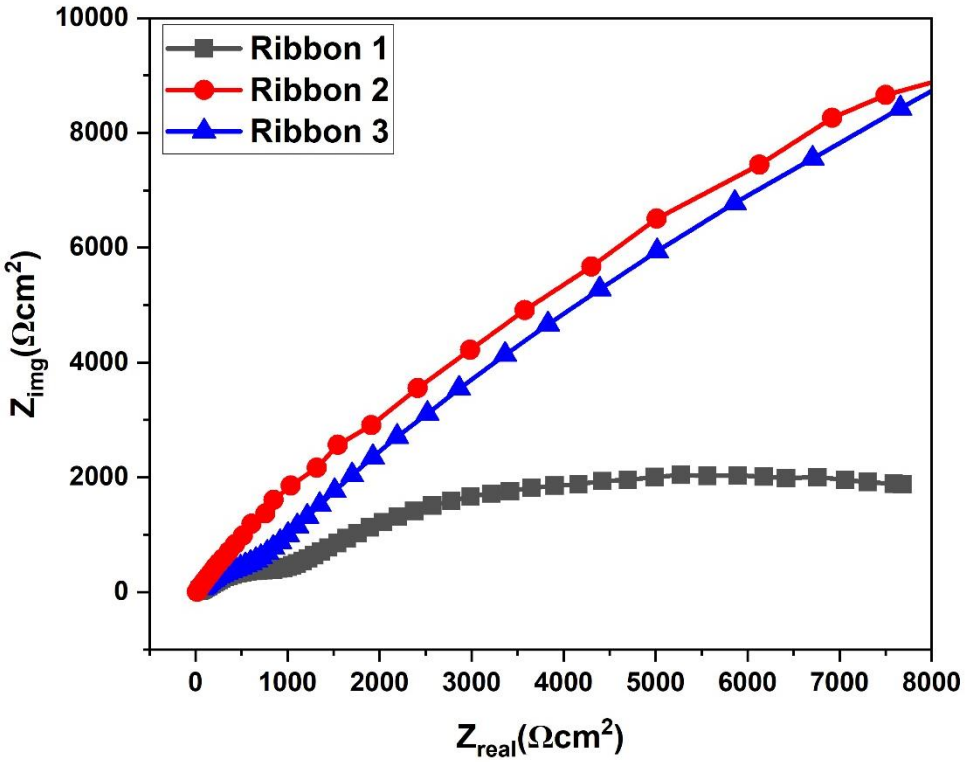

Figure 4.8: EIS Nyquist plot of Ribbon samples exposed to 3.5% NaCl solution.

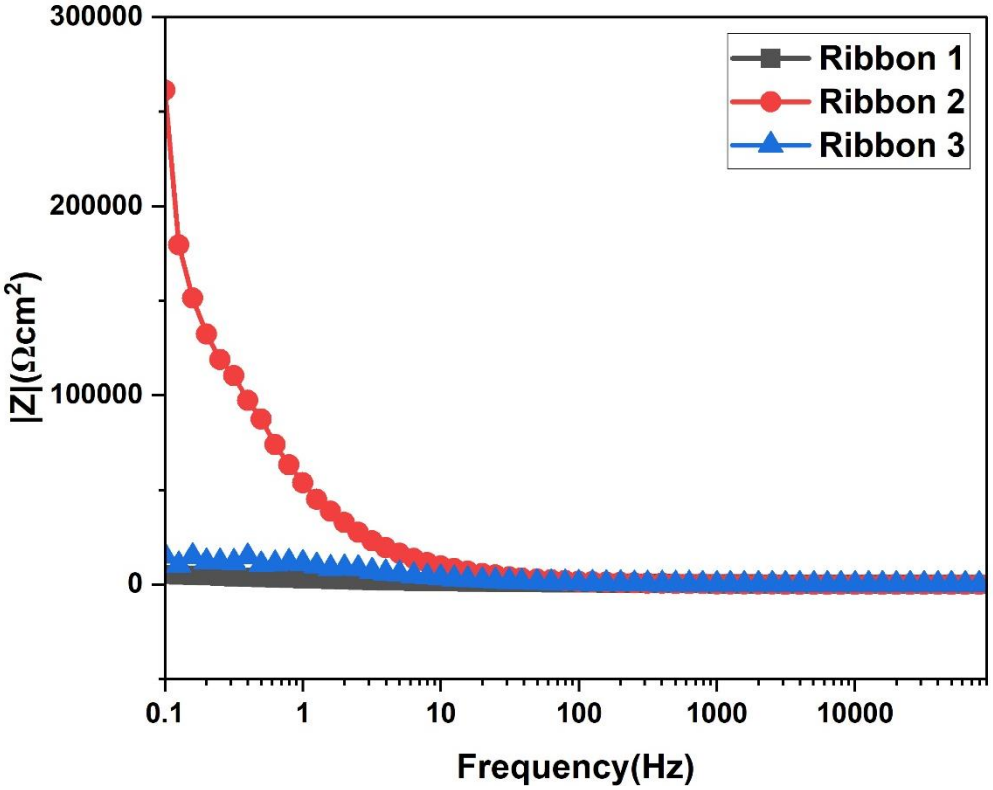

Figure 4.9: EIS Bode impedance plot of Ribbon samples exposed to 3.5% NaCl solution.

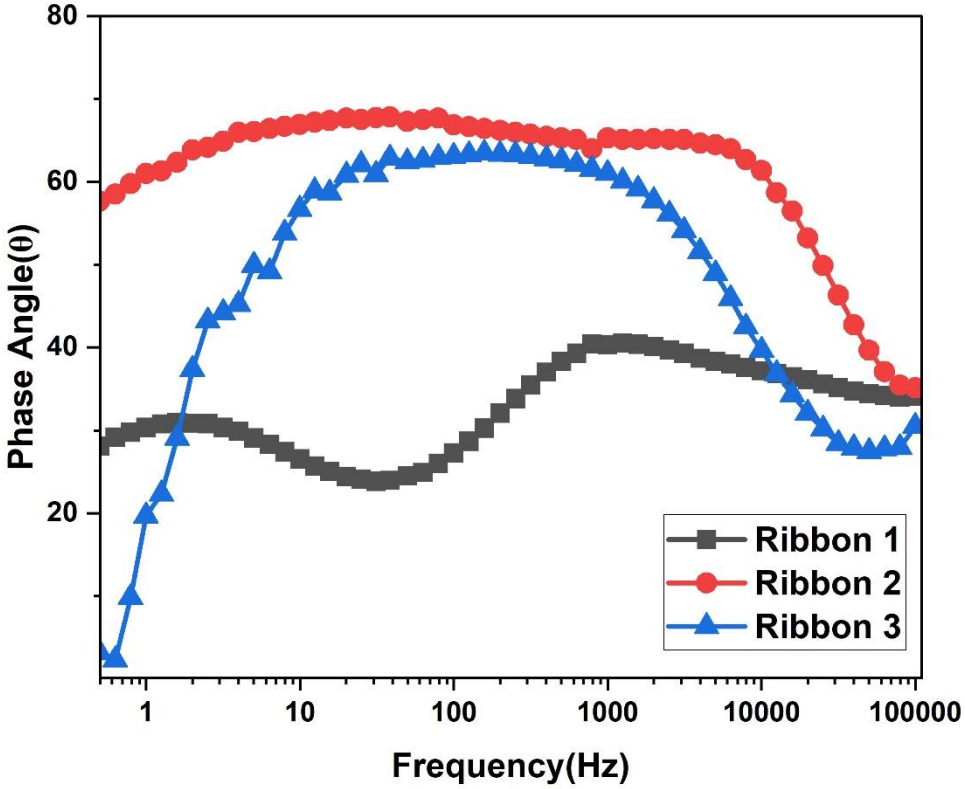

Figure 4.10: EIS Bode phase angle plot of Ribbon samples exposed to 3.5% NaCl solution.

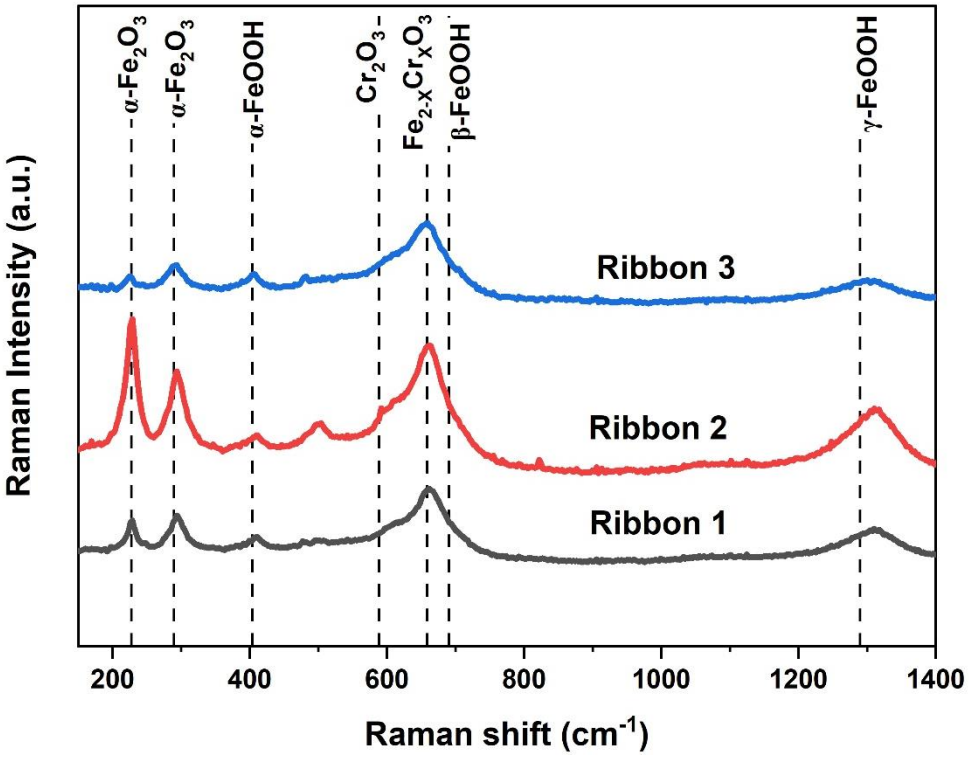

Figure 4.11: Raman spectra of the coating Ribbon sample displaying characteristic peaks of various oxides and hydroxide phases.

Furthermore, Raman spectroscopy was employed to investigate and identify the corrosion products that developed on the surface of the ribbon samples following the electrochemical polarization tests. The Raman spectra obtained for these corroded surfaces are presented in Figure 4.11, providing critical insights into the nature and composition of the rust layers formed as a result of exposure to the corrosive environment. The identified peaks corresponded to various iron and chromium oxide phases, including hematite (α-Fe_2O_3), goethite (α-FeOOH), chromium oxide (Cr_2O_3), chromium-doped hematite ($Fe_{2-x}Cr_xO_3$), as well as the iron oxyhydroxide phases akaganeite (β-FeOOH) and lepidocrocite (γ-FeOOH). The presence of chromium in the Cr_2O_3 and $Fe_{2-x}Cr_xO_3$ phases among the detected compounds indicates their strong barrier properties against corrosion. As illustrated in Figure 4.11, the corrosion products formed on the surface of Ribbon 2 are predominantly composed of Cr_2O_3 and $Fe_{2-x}Cr_xO_3$, with a smaller fraction of α-Fe_2O_3 [14-18].

4.5. Comparative Analysis

In order to gain a deeper understanding of the corrosion resistance behaviour of Fe-based metallic glass coatings, a comparative study was carried out between two samples Coating 2 and Coating 4 each having distinct compositional and structural attributes. Coating 2 demonstrated superior corrosion resistance in preliminary electrochemical tests. To evaluate whether this behaviour was influenced solely by composition or also by the fabrication conditions, Coating 4, prepared using the same processing parameters as Coating 2, was selected for comparison. The detailed compositions of both coatings are presented in the corresponding table.

To further extend this investigation, a ribbon sample with the same nominal composition as Coating 4 $Fe_{80}Cr_{10}B_4C_2P_4$ (at.%) as studied in the previous section, Ribbon 2 was selected for comparative study. This additional sample allowed for the comparison between a fully amorphous bulk form and the corresponding coating material. By doing so, the study aimed to assess whether corrosion resistance differs significantly when the same alloy system is used in a ribbon form (with a typically higher degree of amorphization) versus a thermally sprayed coating, which may exhibit partial crystallinity due to the nature of the deposition process. This study provides a foundational framework for future research into the scalability and adaptability of Fe-based metallic glass systems in both coated and bulk forms, and highlights the importance of process-structure-property relationships in corrosion performance. Figure 4.12 illustrates the potentiodynamic polarization curves of Coating 2, Coating 4, and Ribbon 2 in a 3.5 wt% NaCl solution to systematically characterize the corrosion behavior. The curves were analyzed to extract the corrosion potential (Ecorr) and corrosion current density (icorr) values, which are essential for predicting the corrosion resistance properties of both the coating and the ribbon 1 sample. It was observed that the ribbon has an icorr value of 0.0116 $\mu A/cm^{-2}$, followed by Coating 2 with a value of 9.7 $\mu A/cm^{-2}$, and Coating 4 with an icorr value of 12.1 $\mu A/cm^{-2}$. The ribbon sample exhibited the most noble corrosion potential and the lowest corrosion density, indicating superior resistance to localized corrosive attack compared to the other samples. This suggests that the bulk form of the same composition shows superior corrosion resistance than the coating [12-14].

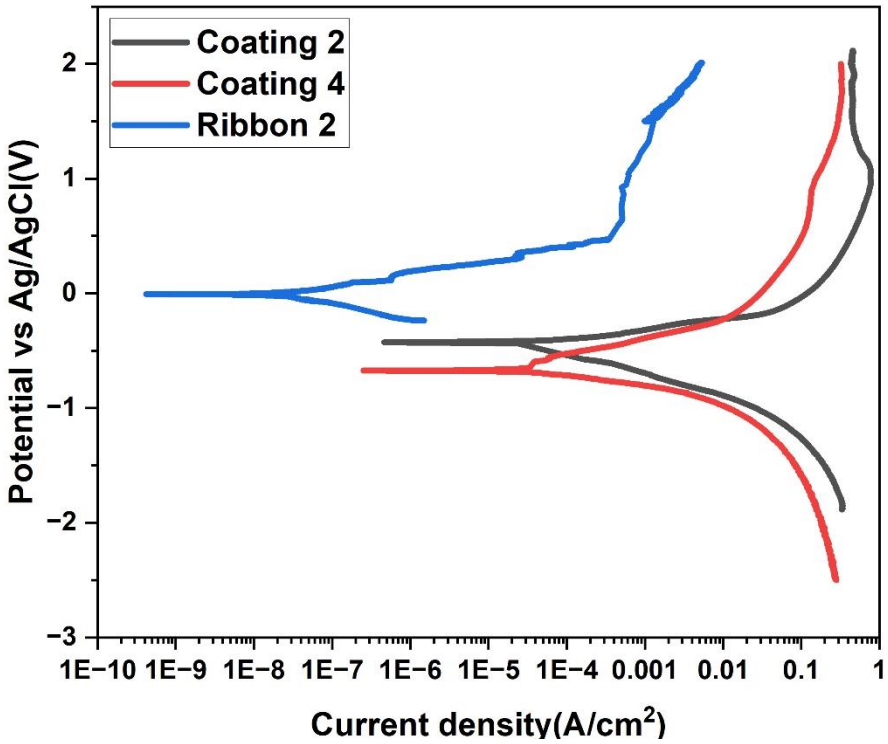

Figure 4.12: Potentiodynamic polarization curves of coated samples and Ribbon sample.

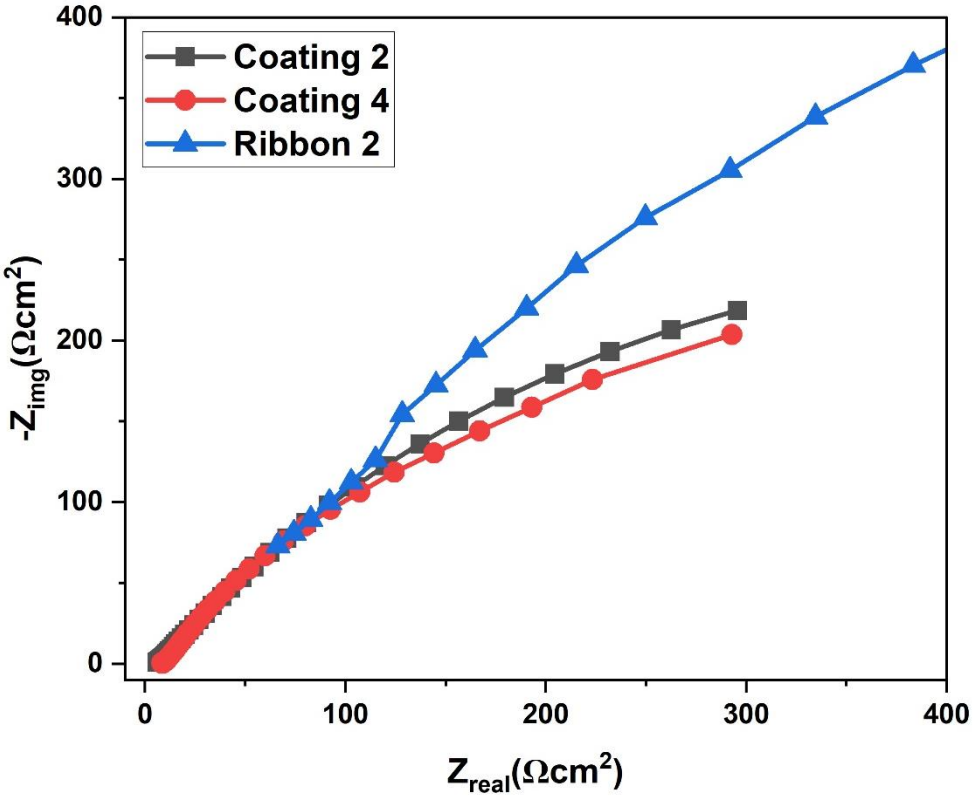

Figure 4.13: EIS Nyquist plot of coatings and ribbon exposed to 3.5% NaCl solution.

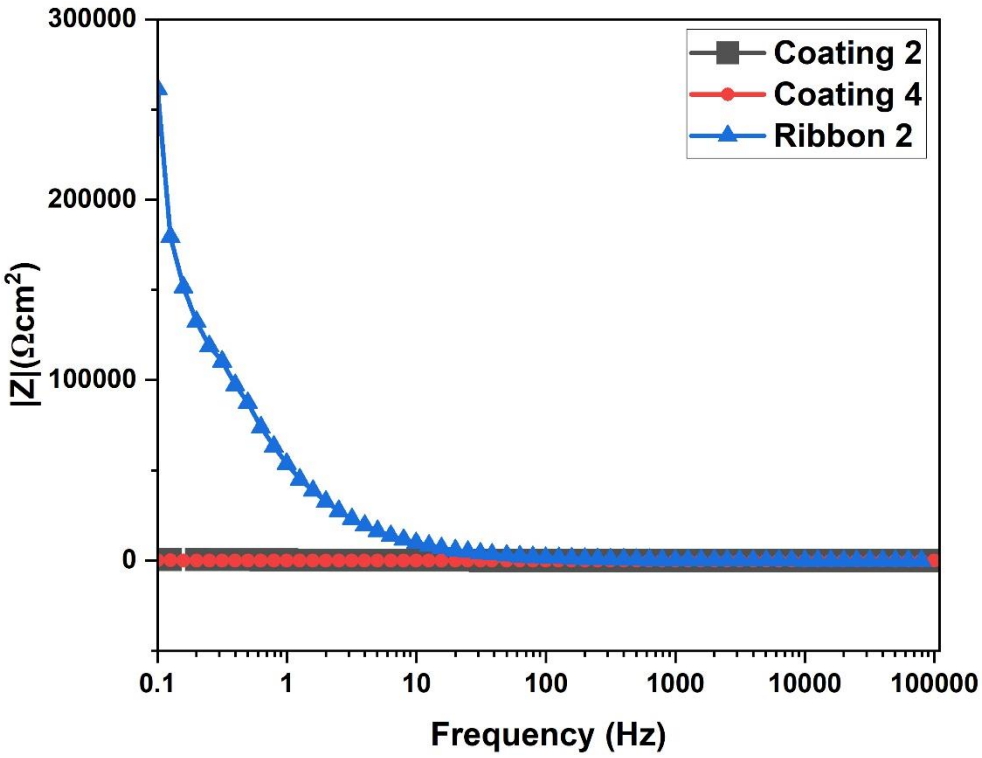

Figure 4.14: EIS Bode impedance plot of coatings and ribbon exposed to 3.5% NaCl solution.

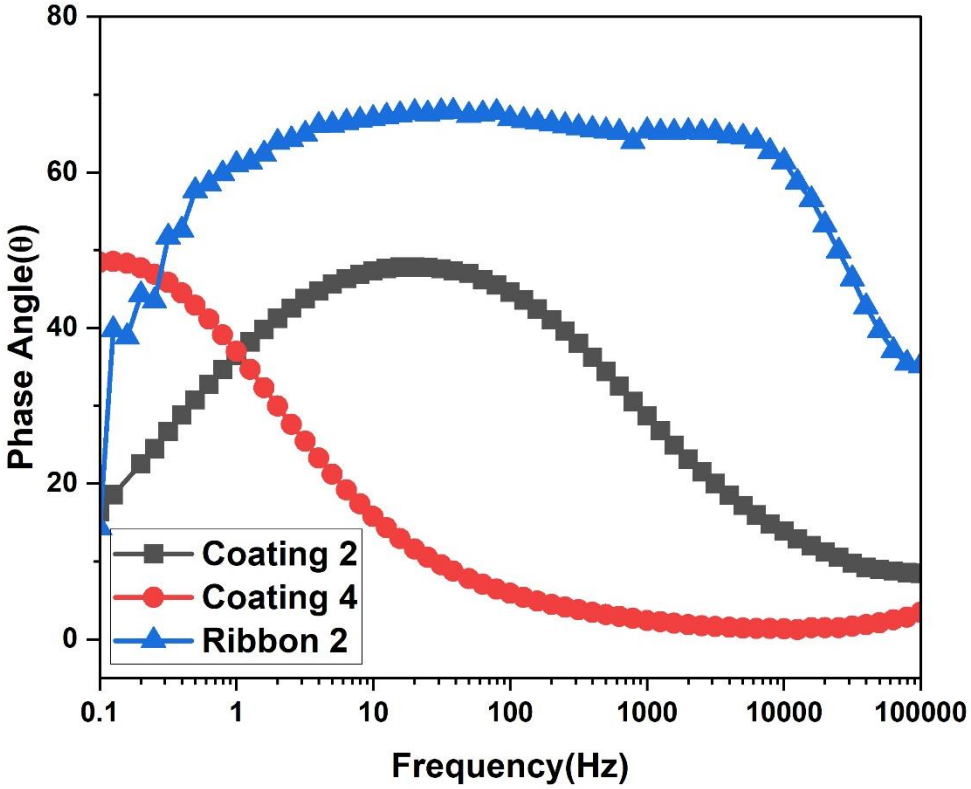

Figure 4.15: EIS Bode phase angle plot of coatings and ribbon exposed to 3.5% NaCl solution.

Electrochemical impedance spectroscopy (EIS) measurements further corroborate these conclusions. In the Nyquist plots (Figure 4.13), Ribbon showed the largest semicircular arc among all samples. A larger R_{ct} implies that the passive film is more resistive to ion transport, indicating a more protective barrier against corrosion [23]. In the Bode magnitude plots (Figure 4.14), Ribbon 1 maintained the highest impedance at low frequencies, reflecting its superior resistive behaviour against electrochemical attack. Moreover, the Bode phase-angle plot (Figure 4.15) for Ribbon exhibited a broad peak near 67.69°, characteristic of a dominant capacitive response over a wide frequency range. This high, broad phase-angle peak indicates a compact and stable passive layer formed on the surface. Together, the polarization and impedance analyses confirm that Ribbon 2 shows the highest corrosion resistance [27].

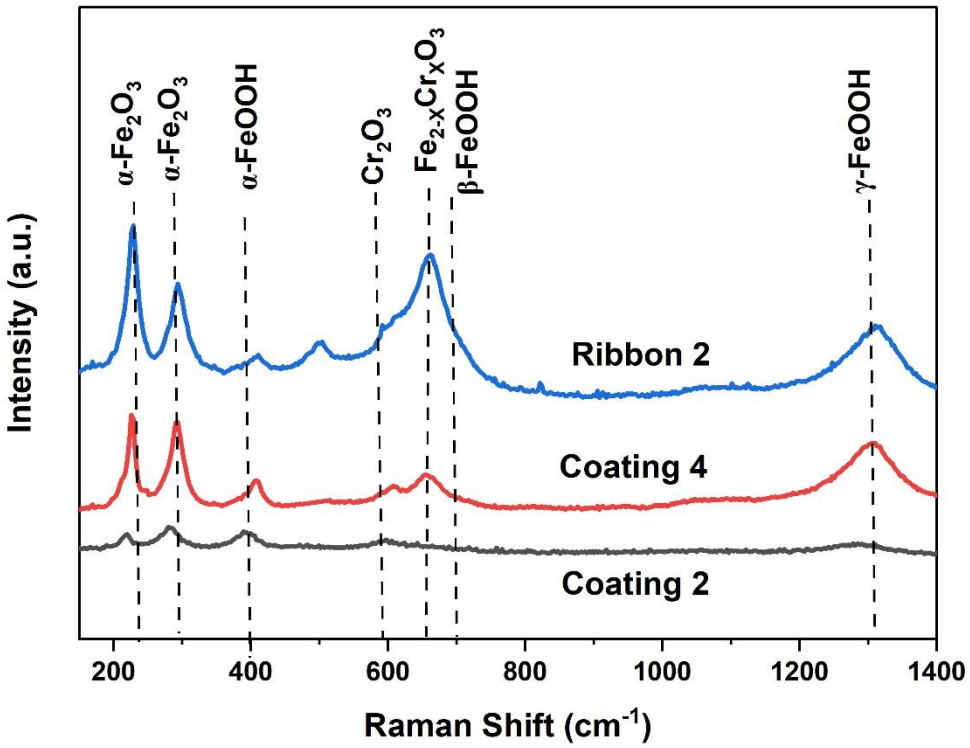

Figure 4.16: Raman spectra of coating 2, 4, and Ribbon sample displaying characteristic peaks of various oxides and hydroxide phases.

Raman spectroscopy was employed to investigate and identify the corrosion products that developed on the surface of the coated samples following the electrochemical polarization tests [20]. The Raman spectra obtained for these corroded surfaces are presented in Figure 4.16, providing critical insights into the nature and composition of the rust layers formed as a result of exposure to the corrosive environment.

The spectral analysis revealed distinct peaks corresponding to akaganeite (β-FeOOH), lepidocrocite (γ-FeOOH), and goethite (α-FeOOH). These compounds are well-known corrosion products associated with the oxidative degradation of iron-based materials in saline media. Among these, β-FeOOH and γ-FeOOH are classified as oxyhydroxide phases that tend to form under high humidity and chloride-rich conditions [14]. These phases are known for their relatively poor structural stability and higher solubility, particularly in environments with elevated salinity, such as marine atmospheres or saline solutions. As a result, their presence typically indicates an accelerated corrosion process. In contrast, α-Fe_2O_3 (hematite), an iron oxide phase, is more stable and generally considered less reactive under similar conditions. A higher concentration of maghemite in the corrosion product layer is often associated with improved passivation and better corrosion resistance. However, in the case of Coating 4, the Raman spectra indicated a lower fraction of γ-Fe_2O_3 and a predominantly higher fraction of β-FeOOH and γ-FeOOH phases [12]. This compositional imbalance in the rust layer suggests that Coating 4 exhibited reduced resistance to the corrosive environment. The dominance of unstable oxyhydroxide phases implies that the passive film formed was not sufficiently protective, thereby allowing

sustained electrochemical degradation. Consequently, the findings support the conclusion that Coating 4 performs poorly in terms of corrosion resistance compared to Coatings 2 and Ribbon 2 evaluated in this study [13].

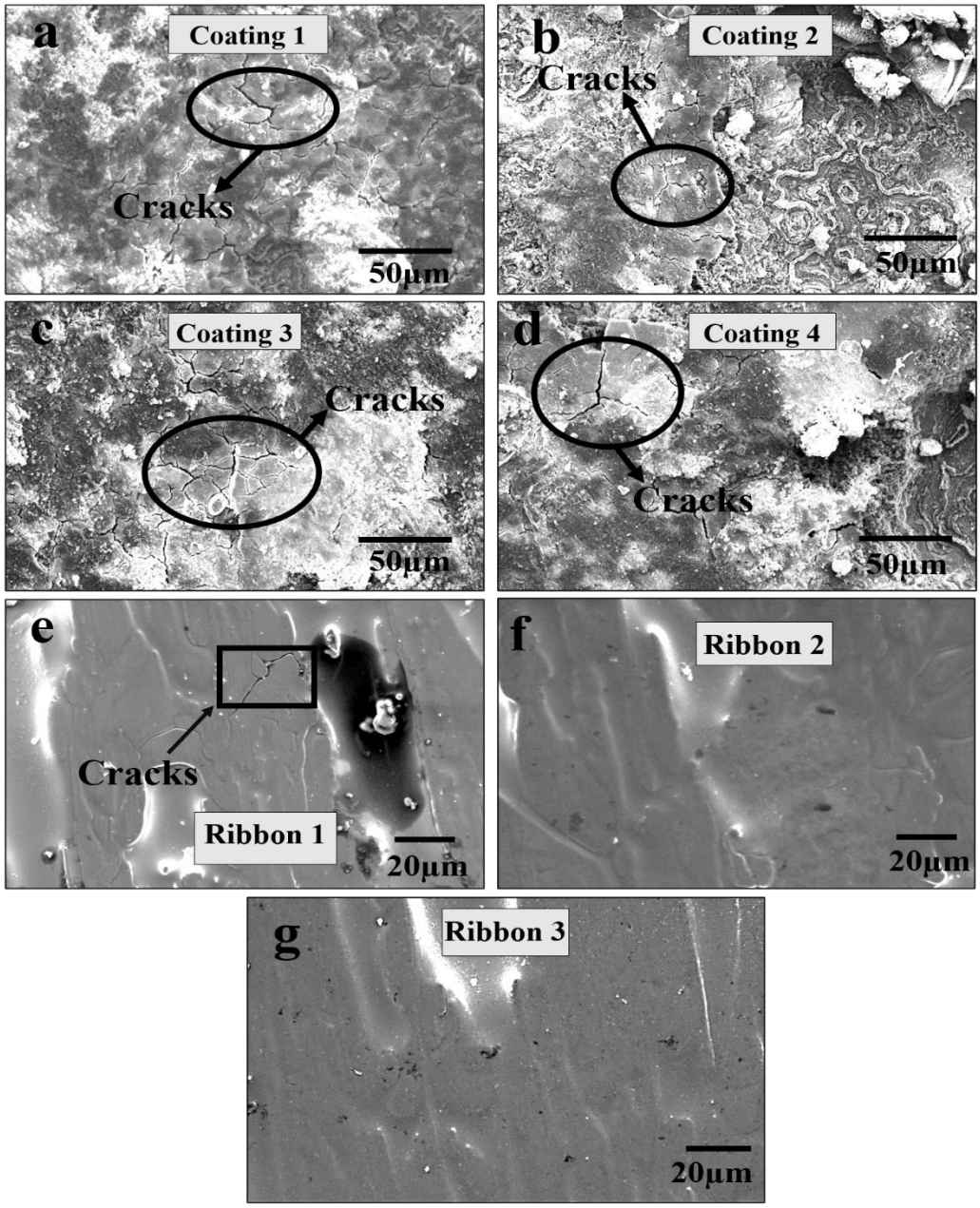

Figure 4.17: SEM micrographs of the surface of Fe-based (a-d) coatings and (e-g) ribbons.

samples and the metallic glass ribbon 1 after undergoing corrosion testing in a 3.5 wt.% NaCl solution. The surface morphology of Coating 1 (Figure 4.17a), Coating 2 (Figure 4.17c), and Coating 3 (Figure 4.17d) clearly exhibits pronounced crack formations and localized corrosion damage. These features are indicative of significant degradation following exposure to the saline environment. In contrast, the surface of Coating 2 shown in Figure 4.17b displays comparatively fewer and less severe cracks, suggesting that this particular coating demonstrated superior resistance to chloride-induced corrosion [18].

The improved corrosion performance of Coating 2 aligns well with the electrochemical characterization data discussed in the preceding sections, particularly the lower corrosion current density (icorr) and the higher charge transfer resistance (Rct) values obtained from potentiodynamic polarization and electrochemical impedance spectroscopy (EIS) measurements [17]. These electrochemical indicators collectively point to a more stable passive film formation and slower corrosion kinetics in Coating 2, which explains its relatively undamaged post-corrosion morphology [29–31]. Furthermore, Figure 4.17e shows the post-corrosion surface of the Fe-based metallic glass ribbon (Ribbon 2), which reveals only a fine, hairline crack and minimal surface degradation, and in Figure 4.17f (Ribbon 2) and g (Ribbon 3) shows no cracks. This observation implies that the ribbon possesses even better corrosion resistance compared to Coating 2. The limited crack development on the ribbon surface indicates high structural integrity and the inherent corrosion-resistant nature of amorphous alloys due to their homogeneous microstructure and lack of grain boundaries [32-34]. This performance is consistent with the previously discussed electrochemical results, reinforcing the superior passive behavior of the ribbon in aggressive chloride environments.

Overall, the microstructural evidence obtained from the post-corrosion analysis supports the conclusions drawn from the electrochemical studies, confirming that Coating 2 exhibits enhanced corrosion resistance characteristics relative to the other coating variants and the Fe-based metallic glass ribbon exhibits superior corrosion resistance characteristics relative to Coating 2. These findings highlight the potential of optimized amorphous coatings and ribbons for use in marine and chloride-rich environments where corrosion resistance is critical [18].

CHAPTER 5

5. Conclusion

5.1. Summary of Key Finding

This research investigated the influence of plasma spray parameters on the microstructure and corrosion performance of Fe-based metallic glass coatings developed using low-chromium and cost-effective compositions. Two alloy systems, $Fe_{73}Cr_2Si_{11}B_{11}C_3$ and $Fe_{80}Cr_{10}B_4C_2P_4$ (at.%), were deposited onto mild steel substrates through atmospheric plasma spraying (APS) at plasma power levels of 25 kW, 30 kW, and 35 kW. The aim was to evaluate how variations in thermal input affect porosity, amorphous phase retention, and corrosion behaviour.

The coatings exhibited a clear trend where increased plasma power improved particle melting and splat bonding, resulting in reduced porosity [25]. Porosity measurements showed a decline from approximately 10 vol.% at 25 kW to 8 vol.% at 30 kW, and further to 5 vol.% at 35 kW. However, a trade-off was observed between coating density and amorphous content. As the plasma power increased, the retained amorphous phase decreased from 90% at 25 kW to 84% at 30 kW, and further down to 75% at 35 kW, due to partial devitrification caused by higher heat input [12].

Electrochemical analysis through potentiodynamic polarization and electrochemical impedance spectroscopy (EIS) confirmed that the coating deposited at 30 kW displayed the most favorable corrosion resistance. It recorded the lowest corrosion current density of 9.7 $\mu A/cm^{-2}$ and the noblest corrosion potential of –485 mV [11]. This coating also exhibited the largest semicircle diameter in the Nyquist plot and the highest low-frequency impedance and phase angle in Bode plots, indicating stable passivation behavior and superior resistance to localized corrosion.

In contrast, while the coating deposited at 25 kW retained the highest amorphous content, its higher porosity adversely affected corrosion performance. Similarly, the coating sprayed at 35 kW, despite its lower porosity, showed inferior corrosion resistance due to increased crystalline content that disrupted passive film stability.

Additionally, a melt-spun ribbon of $Fe_{80}Cr_{10}B_4C_2P_4$ was fabricated to serve as a fully amorphous benchmark. It exhibited significantly better corrosion performance, with a corrosion current density of only 0.0116 $\mu A/cm^{-2}$, highlighting the benefits of complete amorphousness and defect-free structure.

5.2. Future Work

Though the thesis addresses certain basic questions in an area of tremendous applied interest, it also brings out additional questions and scope for further/future research. A few selective suggestions are made as follows:

- To investigate the wear and tribological studies of the coating samples manufactured at different plasma spray parameters and compare them.
- To study the thermodynamic factor for good coating for corrosion resistance.
- To investigate the post-corrosion products for a better understanding of the corrosion behaviour of coating samples.
- To investigate other metallic glass systems for wear and corrosion resistance.
- To evaluate the durability and longevity of the coatings in a corrosive environment by salt spray and cyclic corrosion testing to simulate real-world conditions.
- To integrate the Fe-based metallic glasses with multilayer or composite coating systems.

CHAPTER 6

6.References

1. Budhani R. C., Goel T. C., Chopra K. L., December 1982, Melt-spinning technique for preparation of metallic glasses, Bull. Mater. Sci., pp. 549-561.

2. Öztürk Sultan, Sünbül Sefa Emre, İcin Kürşat, May 2020, Effects of melt spinning process parameters and wheel surface quality on production of 6060 aluminium alloy powders and ribbons, Transactions of Nonferrous Metals Society of China, Pages 1169-1182

3. Li H.X., Lu Z.C., Wang S.L., Wu Y., Lu Z.P., June 2019, Fe-based bulk metallic glasses: Glass formation, fabrication, properties and applications Progress in Materials Science, Pages 235-318

4. Shirzadi A.A., Kozieł T., Cios G., Bala P., February 2019, Development of Auto Ejection Melt Spinning (AEMS) and its application in fabrication of cobalt-based ribbons, Journal of Materials Processing Technology, Pages 377-381

5. Suryanarayana, C., Inoue, A., 2013. Iron-based Bulk Metallic Glasses. International Materials Review 58(3), p 131-166.

6. Tkatch V., Limanovskii A. I., Denisenko S. N., January 2002, The effect of the melt-spinning processing parameters on the rate of cooling, Materials Science and Engineering, p 323(1)

7. Guo S. F., Chan K. C., Xie S. H., Yu Peng, Hung Y. J., Zhang H. J., June 2013, Novel centimeter-sized Fe-based bulk metallic glass with high corrosion resistance in simulated acid rain and seawater, Journal of Non-Crystalline Solids, p 369

8. Gupta R. K., Kumar D., & Balani K., April 2017, Corrosion resistance of plasma-sprayed Fe-based amorphous coatings, Journal of Thermal Spray Technology, 26(4), pp. 656–665.

9. Zhou Y., Li J., Wang Q, December 2014. Atmospheric plasma sprayed Fe-based metallic glass coatings: Structure and corrosion resistance, Surface and Coatings Technology, 258, pp. 922–928.

10. Li Y., Zhang Y., Zhang H., December 2009. Novel centimeter-sized Fe-based bulk metallic glass with high corrosion resistance in simulated acid rain and seawater, Corrosion Science, 51(12), pp. 2979–2983.

11. Souza C.A.C., Ribeiro D.V., Kiminami C.S.. 2016. Corrosion Resistance of Fe-based Amorphous Alloy: An Overview. Journal of Non-Crystalline Solids 442, 56-66

12. Kumar A., Nayak S., Bijalwan P., Dutta M., Banerjee A., Laha T., 2019. Optimization of mechanical and corrosion properties of plasma sprayed low chromium containing Fe-based amorphous/nanocrystalline composite coating. Surface & Coatings Technology 370, 255-268

13. Nayak S., Kumar A., Sarkar K., Pathak A., Banerjee A., Laha T., 2019. A Study on the Corrosion Inhibition of Fe-Based Amorphous/ Nanocrystalline Coating Synthesized by High-Velocity Oxy Fuel Spraying in an Extreme Environment. J Therm Spray Tech 28:1433–1447

14. Kumar A., Nayak S., Sarkar K., Banerjee A., Mondal K., Laha T., 2020. Investigation of nano- and micro-scale structural evolution and resulting corrosion resistance in plasma sprayed Fe-based (Fe-Cr-B-C-P) amorphous coatings. Surface & Coatings Technology. 397, 126058

15. Liu X.Q., Zheng Y.G., Chang X.C., Hou W.L., Wang J.Q., Tang Z., Burgess A., 2009. Microstructure and properties of Fe-based amorphous metallic coating produced by high velocity axial plasma spraying. Journal of Alloys Compounds. 484, 300–307.
16. An Y., Hou G., Chen Jie., Zhao X., Liu G. Zhou H., Chen J., 2014. Microstructure and tribological properties of iron-based metallic glass coatings prepared by atmospheric plasma spraying, Vacuum 107, 132–140.
17. Kumar A., Nayak S., Bijalwan P., Dutta M., Banerjee A., Laha T., 2019. Mechanical and corrosion properties of plasma sprayed Fe-based amorphous/nanocrystalline composite coating. Advances In Materials and Processing Technologies. 2019.1598129
18. Nayak S., Kumar A., Sarkar K., Banerjee A., Laha T., 2020. Mechanistic insight into the role of amorphicity and porosity on determining the corrosion mitigation behavior of Fe-based amorphous/nanocrystalline coating. Journal of Alloys and Compounds 849,156624
19. Yang Y., Zhang C., Zhang Y. x., Yu Y., Liu L., 2012. Effects of crystallization on the corrosion resistance of Fe-based amorphous coatings. Corrosion Science 59 (2012) 10-19
20. De La Fuente D., Alcantara J., Chico B., Díaz I., Jimenez J.A., Morcillo M., 2016. Characterisation of rust surfaces formed on mild steel exposed to marine atmo spheres using XRD and SEM/Micro Raman techniques, Corrosion Sci. 110, 253-264
21. Zhang, Guan, March 2022, Multicomponent Fe-Based Bulk Metallic Glasses with Excellent Corrosion and Wear Resistances, Metals, 12(4), Article 564.
22. Zhu, Chun-lei, June 2010, Formation and Corrosion Properties of Fe-Based Bulk Metallic Glasses, International Journal of Minerals, Metallurgy and Materials, 17(3), pp. 323–326.
23. Asami, Katsuhiko, November 2007, Corrosion Resistance of Metallic Glasses, Journal of the Japan Society of Powder and Powder Metallurgy, 54(11), pp. 795–800.
24. Han, Huawei, November 2023, Corrosion Performance of Fe-Based Amorphous Coatings via Laser Cladding Assisted with Ultrasonic in a Simulated Marine Environment, Metals, 13(12), Article 1938.
25. Zarazúa-Villalobos, L., November 2021, Microstructure and Corrosion Study of Fe-Based Bulk Metallic Glass Obtained by Spark Plasma Sintering, Journal of Alloys and Compounds, 880, Article 160399.
26. Zhang, Chang Lai, September 2018, Fe-Based Metallic Glasses in Functional Catalytic Applications, Chemistry – An Asian Journal, 13(23), pp. 3575–3592.
27. Stoica, Mihai, February 2017, Fe-Based Bulk Metallic Glasses: Understanding the Influence of Impurities on Glass Formation, Springer Wiesbaden, pp. 1–126.
28. Patel S. K., Swain B. K., Behera A., January 2020, Metallic Glasses: A Revolution in Material Science, IntechOpen, Chapter.
29. Zhang, X., March 2015, Electrochemical behavior and corrosion resistance of Fe-based amorphous coatings in NaCl solutions, Corrosion Science, pp. 213–222.
30. Qiu J., July 2018, Enhanced corrosion protection of Fe-based metallic glass coatings by nanostructured surface modifications, Electrochimica Acta, pp. 98–107.
31. Li, Y., December 2020, Corrosion performance of Fe-based amorphous coatings: Influence of alloying elements and surface characteristics, Journal of Alloys and Compounds, pp. 452–462.

32. Inoue A., September 2000, Stabilization of metallic supercooled liquid and bulk amorphous alloys, Materials Transactions, pp. 291–302.
33. Chen, H.S., June 1974, Thermal stability and glass-forming ability of metallic glasses, Acta Metallurgica, pp. 1505–1511.
34. Guo S., November 2019, Corrosion resistance of Fe-based bulk metallic glasses in various chloride environments, Materials Chemistry and Physics, pp. 208–216.
35. Greer A. L., Costa M. B., Houghton O. S., October 2023, Metallic glasses, MRS Bulletin, Volume 48, pages 1054–1061.
36. Inoue, A., 2000, Stabilization of metallic supercooled liquid and bulk amorphous alloys. Acta Materialia, 48(1), 279–306.
37. Schuh, C. A., Hufnagel, T. C., & Ramamurty, U., 2007, Mechanical behavior of amorphous alloys. Acta Materialia, 55(12), 4067–4109.
38. Guo, H., et al., 2007, Passive film formation on Fe-based amorphous alloys. Corrosion Science, 49, 2724–2731.
39. Ahn, S. J., et al., 2005, Role of Cr and Mo in Fe-based amorphous alloys. Journal of Alloys and Compounds, 400, 91–98.
40. Pardo, A., et al., 2008, Influence of alloying elements on passive films. Corrosion Science, 50(7), 1796–1806.
41. Zhang, T., et al., 2004, Boron effect on passivation in Fe–B–Si systems. Materials Transactions, 45(4), 1166–1171.
42. Wang, X., et al., 2006, Electrochemical corrosion of Fe–Cr–Mo–B metallic glass. Electrochimica Acta, 52(3), 800–808.
43. Li, H., et al., 2015, EIS study of corrosion of Fe-based BMG. J. Mater. Sci. Technol., 31(8), 773–780.
44. Kimura, H., et al., 2002, Crystallization and corrosion behavior of Fe–Cr–Mo–C–B alloy. Materials Transactions, 43(9), 2325–2329.
45. Shimizu, Y., 2006, Passive film breakdown of metallic glasses in acid media. Electrochimica Acta, 52, 174–180.
46. Schroers, J., 2005, Devitrification and corrosion in Fe-based MGs. Applied Physics Letters, 87(6), 061912.
47. Kim, Y. C., et al., 2005, Corrosion behavior of Fe–B–Si–Nb amorphous alloys in NaCl solution. Journal of Non-Crystalline Solids, 351(6–7), 482–488.
48. Zhang, T., et al., 2003, Electrochemical corrosion behavior of Fe-based bulk metallic glasses in acidic and chloride-containing solutions. Materials Transactions, 44(10), 2011–2014.
49.R. M. German, Powder Metallurgy Science, 2nd ed., Metal Powder Industries Federation (MPIF), Princeton, NJ, 1994, ISBN-13: 978-1878954428.)
50. Ouyang G., Chen X., Liang Y., Macziewski., Cui J., July 2019, Review of Fe-6.5 wt%Si high silicon steel A promising soft magnetic material for sub-kHz application, Journal of Magnetism and Magnetic Materials, Volume 481, Pages 234-250.
51.TailorS., Soni P.R., 2010, Plasma Spray Coatings: State of the Art, ResearchGate Publication.
52.Hou G., An Y., Liu G., Zhou H., Chen J., Chen Z., 2011, Effect of Atmospheric Plasma Spraying Power on Microstructure and Properties of WC-$(W,Cr)_2C$-Ni Coatings, Journal of Thermal Spray Technology, Vol-20, 1150–1160.

सर मोक्षगुंडम विश्वेश्वरय्या